LA-UR-95-1146

Los Alamos National Laboratory is operated by the University of California for the United States Department of Energy under contract W-7405-ENG-36

TITLE: **CURVILINEAR COORDINATES FOR GLOBAL OCEAN MODELS**

AUTHOR(S): R(ichard) D. Smith , T-3
S(amuel) Kortas , Univ. Aix-Marseille
B(ertrand) Meltz , CEA/VALENTON

SUBMITTED TO: *Journal of Computational Physics*

Los Alamos

Los Alamos National Laboratory
Los Alamos, New Mexico 87545

FORM NO. 836 R4
ST. NO. 2629 5/81

Curvilinear Coordinates for Global Ocean Models

Richard D. Smith

Theoretical Division, Group T-3, Los Alamos National Laboratory

University of California, Los Alamos, New Mexico 87545

Samuel Kortas

I.R.P.H.E., UMR 138 C.N.R.S., Universités Aix-Marseille I & II

Equipe Mathématiques Numériques pour la Modélisation

12, Avenue du Général Leclerc, 13003 Marseille, France

Bertrand Meltz

Centre d'Etudes de Limeil-Valenton

Comissariat a l'Energie Atomique

94195 Villeneuve-St-Georges, CEDEX, France

Abstract

A new class of orthogonal curvilinear dipole coordinate systems on the sphere with arbitrarily-located poles is introduced and used to construct computational meshes for global ocean models. These grids can be constructed analytically, and their parameters can be adjusted to satisfy various desirable properties, such as having the grid poles located inside land masses, having a zonal coordinate line along the Equator, and being able to focus high resolution in the subpolar North Atlantic for more accurate modeling of the thermohaline circulation. The primitive equations are derived in generalized orthogonal spherical coordinates and the new grid scheme is implemented in a global ocean general circulation model. Results from eddy-resolving and non-eddy-resolving simulations are presented.

1. Introduction

A standard difficulty encountered in modeling fluid flows on the sphere using finite-difference methods is the so-called "pole problem" associated with the convergence of meridians at the North and South poles. In computational grids whose coordinates are lines of constant longitude and latitude, the cell widths decrease to zero like the cosine of latitude as the poles are approached, and the time step used with explicit time-integration methods must also approach zero. This is the well-known Courant-Friedrichs-Lewy (CFL) stability limit, which restricts the time step to be less than the time taken by the fastest waves or inertial flows in the model to traverse the smallest grid cells. In atmospheric models this problem can be avoided by using spectral transform methods, where the time step is limited only by the maximum zonal wavenumber of a truncated spherical harmonic basis. Global spectral transform methods cannot, however, be applied to ocean modeling because of the complicated lateral boundary conditions associated with coastlines and bottom topography. Hence, ocean models with realistic topography are based on either finite-difference, finite-element, or spectral-element methods.

There are several approaches to overcoming the pole problem in ocean general circulation models (OGCMs). The simplest of these is to eliminate the North Pole by excluding all or part of the Arctic Ocean and cutting off the grid at some high northern latitude (the South Pole is of course not a problem since it is inside Antarctica). However, it is now widely recognized that ocean and sea-ice dynamics in the Arctic play a crucial role in the global climate system [1]. Another possibility is to use fully implicit rather than explicit time-integration techniques, but these involve the solution of multi-dimensional elliptic boundary-value problems which are computationally expensive and very difficult to solve numerically. The more common approach in global models is to smooth the solution at high latitudes using one-dimensional filtering along constant latitude ocean segments near the pole [2], but this is also expensive and may corrupt the solution or

destroy important properties of a field such as $\nabla \cdot \mathbf{u} = 0$. Filtering and implicit methods are also difficult to parallelize and hence are less useful for high-resolution global models designed to run on massively parallel computers (MPPs). They generally involve nonlocal communication, and the North Pole remains a unique point requiring special treatment (e.g., cross-pole advection).

The final possibility for overcoming the pole problem is to use a coordinate transformation which either eliminates the poles or displaces them into land masses. Grids obtained by rotating the standard polar grid to displace the singularities out of the region of interest have been used to model the Arctic Ocean [3]. However, a simple rotation is inadequate for a global model since there are no large antipodal land masses on the Earth that can be used to hide both grid singularities. A variation of this approach for global models was recently suggested by Eby and Holloway [1], which uses a rotated grid in the North-Atlantic/Arctic region matched onto a standard polar grid everywhere else.

Many options for more complicated grid transformations are available. Unstructured meshes provide the most general gridding schemes for complicated geometries [4], but they also present the greatest challenge in developing good numerical schemes, particularly on parallel machines, since they typically have a one-dimensional data structure and all communication is via indirect addressing with nonlocal communication. One option is to use spherical tessellations. These are nonorthogonal grids, but they do retain a 2-D horizontal data structure and provide for nearly uniform cell widths over the globe. This approach has been used successfully to model 3-D mantle convection using finite-element methods [5] but has had limited application in meteorology [6,7]. Another option for atmospheric models is the use of "stretched" grids [8] with global spectral-transform methods. These grids allow resolution to be focused near one of the two diametrically-opposed poles and are typically rotated to obtain high resolution in a select region.

In this paper we are primarily concerned with investigating orthogonal curvilinear coordinate systems on the surface of the sphere. We will restrict ourselves to "dipole"

coordinate systems: those with two grid singularities, or "grid poles", which may be located anywhere on the surface. Such grids have the same topology as the standard polar grid and share many of its desirable features, as discussed below. Other methods such as filtering, implicit methods, or the use of nonorthogonal grids, do not present insurmountable technical problems, but our approach is to avoid these problems by finding a simple orthogonal coordinate system that has most of the essential features needed in a global ocean grid.

Let us first consider what are the important physical, numerical, and computational issues that arise in selecting or designing such a grid?

Physical: The main physical features effecting horizontal grid resolution are: 1) the complex topography, which strongly influences the pathways of ocean currents; 2) the narrow western boundary currents (tens of kilometers wide) that are responsible for poleward transport of heat and salt; 3) the relatively narrow (100–200 km) zonal equatorial current systems and linear waves in the equatorial waveguide, and 4) in eddy-resolving models, the characteristic length scale of the dominant instability mechanism, which is smaller at higher latitudes. This length scale is the Rossby deformation radius $R_1 = C_g/f$ which depends on the Coriolis parameter f and the gravity-wave speed C_g of the first internal mode (typically C_g is of order 1–3 m/sec, and R_1 ranges from about 60 km at 20° to less than 10 km at latitudes greater than 60°). In short, we would like to have resolution focused near western boundaries, at high latitudes, and to a lesser degree near the Equator. From the point of view of studying long-term climate variability [9], we would also like to have reasonably high resolution in the North-Atlantic and the subpolar deep-water formation regions for modeling the thermohaline circulation (THC).

Numerical: In order to employ simple and accurate numerical algorithms, we would like the grid to have the following properties: 1) no grid poles near ocean points, to avoid overly-restrictive CFL limits due small cell widths; 2) it should be able to support the second-order spatial accuracy of the finite-difference schemes typically employed in OGCMs; 3) we

would prefer that one coordinate should be along the zonal direction in the Equatorial region in order to obtain accurate finite-difference dispersion relations for the linear waves (particularly Kelvin waves which play an important role in modeling El Niño); these are much less accurate along diagonal directions in the mesh [10]; 4) for simplicity we would prefer the grid to be orthogonal and, if possible, to have an analytic representation so that no artificial nonorthogonality will be introduced in the numerical construction of the grid; and finally, 5) we would also like the grid to be a single globally-connected mesh, rather than a composite mesh, in order to avoid interpolation in overlap regions.

Computational: For computational efficiency we would like to have a simple data structure, and for this reason we choose to restrict ourselves to dipole grids, since they can be mapped onto a single cyclic logically 2-D mesh, so that indirect addressing is not required for near-neighbor communication. On parallel machines this data structure also has the largest possible subgrid ratio (the surface-to-volume ratio of data on each processing node) which is generally desirable for enhanced performance on MPPs. More complex data structures associated with composite or multipole grids generally involve explicit looping over patches and a reduced subgrid ratio. The other issue is the ocean-land load imbalance problem, which in parallel ocean models is usually ignored, allowing processors with land points to sit idle or do useless work. For this reason we would like the ratio of ocean to land points in the field arrays to be as large as possible.

In this paper we will present a class of orthogonal 2-D spherical dipole coordinate systems that can be adjusted to satisfy essentially all the desirable properties discussed above for global ocean models. Implementation of such a grid requires an ocean model capable of handling general orthogonal coordinates. In Section 2 the primitive equations for ocean dynamics are derived in general curvilinear coordinates, and the basic finite-difference operators are presented for B- and C-type grids; the implementation in our ocean model, the Parallel Ocean Program (POP), is also discussed. In Section 3 we introduce a simple analytic dipole grid with arbitrarily placed poles that reduces to the standard

polar grid as a special case. In Section 4 we discuss composite generalizations of this basic idea and show that composite grids developed previously by others are special cases of this general framework. The breakdown of second-order accuracy in composite grids is also discussed. Section 5 presents a class of continuous generalizations of the composite grids that support higher-order spatial differencing schemes. In Section 6 the algorithm for numerically constructing such a grid is given, and the parameters defining the system are adjusted to satisfy various desirable properties in a computational mesh with realistic bathymetry. In Section 7 results are shown from two numerical integrations using the POP model: one using a non-eddy-resolving $\langle 2/3^\circ \rangle$ average-resolution grid, and another using an eddy-resolving $\langle 1/3^\circ \rangle$ grid.

2. The Primitive Equations in Generalized Spherical Coordinates

Ocean dynamics are described by the 3-D primitive equations for a thin stratified fluid using the hydrostatic and Boussinesq approximations. The continuous equations in standard polar coordinates (with vertical z-coordinate) are:

momentum equations:

$$\frac{\partial}{\partial t}u + \mathcal{L}(u) - (uv\tan\phi)/a - fv = -\frac{1}{\rho_0 a\cos\phi}\,\frac{\partial p}{\partial \lambda} + \mathcal{F}_{Hx}(u,v) + \mathcal{F}_V(u) \tag{1a}$$

$$\frac{\partial}{\partial t}v + \mathcal{L}(v) + (u^2\tan\phi)/a + fu = -\frac{1}{\rho_0 a}\,\frac{\partial p}{\partial \phi} + \mathcal{F}_{Hy}(v,u) + \mathcal{F}_V(v) \tag{1b}$$

$$\mathcal{L}(\alpha) = \frac{1}{a\cos\phi}\left[\frac{\partial}{\partial\lambda}(u\alpha) + \frac{\partial}{\partial\phi}(\cos\phi\, v\alpha)\right] + \frac{\partial}{\partial z}(w\alpha) \tag{1c}$$

$$\mathcal{F}_{Hx}(u,v) = A_M\left\{\nabla^2 u + u(1-\tan^2\phi)/a^2 - \frac{2\sin\phi}{a^2\cos^2\phi}\,\frac{\partial v}{\partial\lambda}\right\} \tag{1d}$$

$$\mathcal{F}_{Hy}(v,u) = A_M\left\{\nabla^2 v + v(1-\tan^2\phi)/a^2 + \frac{2\sin\phi}{a^2\cos^2\phi}\,\frac{\partial u}{\partial\lambda}\right\} \tag{1e}$$

$$\nabla^2\alpha = \frac{1}{a^2\cos^2\phi}\frac{\partial^2\alpha}{\partial\lambda^2} + \frac{1}{a^2\cos\phi}\frac{\partial}{\partial\phi}\left(\cos\phi\frac{\partial\alpha}{\partial\phi}\right) \tag{1f}$$

$$\mathcal{F}_V(\alpha) = \frac{\partial}{\partial z}\mu\frac{\partial}{\partial z}\alpha \tag{1g}$$

continuity equation:

$$\mathcal{L}(1) = 0 \tag{2}$$

hydrostatic equation:

$$\frac{\partial p}{\partial z} = -\rho g \tag{3}$$

equation of state:

$$\rho = \rho(T, S, p) \tag{4}$$

tracer transport:

$$\frac{\partial}{\partial t}T + \mathcal{L}(T) = \mathcal{D}_H(T) + \mathcal{D}_V(T) \tag{5a}$$

$$\frac{\partial}{\partial t}S + \mathcal{L}(S) = \mathcal{D}_H(S) + \mathcal{D}_V(S) \tag{5b}$$

$$\mathcal{D}_H(\alpha) = A_H\nabla^2\alpha \tag{5c}$$

$$\mathcal{D}_V(\alpha) = \frac{\partial}{\partial z}\kappa\frac{\partial}{\partial z}\alpha\,, \tag{5d}$$

where λ, ϕ, $z = r - a$ are longitude, latitude and depth relative to mean sea level $r = a$; g is the acceleration due to gravity, $f = 2\Omega\sin\phi$ is the Coriolis parameter, and ρ_0 is the background density of water. The seven variables in these equations are the two horizontal velocity components (u, v), the vertical velocity w, the pressure p, the density ρ, and the temperature T and salinity S. A_H and A_M are, respectively, the coefficients for horizontal

diffusion and viscosity (here assumed to be constant), and κ and μ are the corresponding vertical coefficients which typically depend on the local Richardson number [11]. The third terms on the left-hand side in Eqs. (1a,b) are due to the convective derivatives in $d\mathbf{u}/dt$ acting on the unit vectors in the λ, ϕ directions, and the second and third terms in Eqs. (1d,e) arise in a transversely-isotropic formulation of the viscosity [12]. The forcing due to wind stress and heat and fresh water fluxes are applied as surface boundary conditions to the friction and dissipative terms $\mathcal{F}$ and $\mathcal{D}$. For more detailed discussion of these equations see for example, [13].

To derive the primitive equations in general coordinates, consider the transformation from Cartesian coordinates (ξ_1, ξ_2, ξ_3 with origin at the center of the Earth) to general horizontal coordinates (q_x, q_y, z), where q_x and q_y are arbitrary curvilinear coordinates in the horizontal directions, and $z = r - a$ is again the vertical coordinate normal to the surface of the sphere. For simplicity of notation in the final equations, we have chosen to denote actual distances along the curvilinear coordinates by x and y, which lie along the circumpolar (longitude-like) and azimuthal (latitude-like) coordinate lines, respectively, on dipole grids with two arbitrarily located poles. The differential length element ds is given by

$$ds^2 = d\xi_1^2 + d\xi_2^2 + d\xi_3^2 = h_{ij} dq_i dq_j + dz^2 \tag{6a}$$

$$h_{ij} = \frac{\partial \xi_k}{\partial q_i} \frac{\partial \xi_k}{\partial q_j} , \tag{6b}$$

(where $i, j = x, y$ and repeated indices are summed). The metric coefficients h_{ij} depend on the local curvature of the coordinates. Differential lengths in the z direction are assumed independent of x and y, so no metric coefficients involving z appear. Further restricting ourselves to orthogonal grids, the cross terms vanish, and we have

$$\begin{aligned} h_i &\equiv h_{ii} , \quad h_{ij} = 0 \ (i \neq j) \\ ds_i &= h_i dq_i . \end{aligned} \tag{7}$$

For the purpose of constructing horizontal finite-difference operators corresponding to the various terms in the primitive equations, define:

$$\begin{aligned} \Delta_i &\equiv ds_i \\ \delta_i &\equiv \frac{\partial}{\partial s_i} = \frac{1}{h_i}\frac{\partial}{\partial q_i} , \end{aligned} \tag{8}$$

where Δ_i and δ_i can be interpreted as either infinitesimal or finite differences and their associated derivatives. Formulas for the basic horizontal operators (gradient, divergence, curl) can be found in standard textbooks [14]. The gradient is

$$\nabla\psi = \hat{\mathbf{x}}\frac{1}{h_x}\frac{\partial\psi}{\partial q_x} + \hat{\mathbf{y}}\frac{1}{h_y}\frac{\partial\psi}{\partial q_y} \tag{9a}$$

$$= \hat{\mathbf{x}}\delta_x\psi + \hat{\mathbf{y}}\delta_y\psi . \tag{9b}$$

where $\hat{\mathbf{x}}$ and $\hat{\mathbf{y}}$ are unit vectors in the x, y directions. The divergence is:

$$\nabla\cdot\mathbf{u} = \frac{1}{h_x h_y}\frac{\partial}{\partial q_x}(h_y u_x) + \frac{1}{h_x h_y}\frac{\partial}{\partial q_y}(h_x u_y) \tag{10a}$$

$$= \frac{1}{\Delta_y}\delta_x(\Delta_y u_x) + \frac{1}{\Delta_x}\delta_y(\Delta_x u_y) , \tag{10b}$$

which gives the form of the continuity equation (Eq. 2) (u_x and u_y are the velocity components along the $\hat{\mathbf{x}}$ and $\hat{\mathbf{y}}$ directions). The advection operator (Eq. 1c) is similar:

$$L(\alpha) = \frac{1}{\Delta_y}\delta_x(\Delta_y u_x\alpha) + \frac{1}{\Delta_x}\delta_y(\Delta_x u_y\alpha) + \delta_z(w\alpha) . \tag{11}$$

The horizontal part (z-component) of the curl operator is

$$\hat{\mathbf{z}}\cdot\nabla\times\mathbf{u} = \frac{1}{h_x h_y}\frac{\partial}{\partial q_x}(h_y u_y) - \frac{1}{h_x h_y}\frac{\partial}{\partial q_y}(h_x u_x) \tag{12a}$$

$$= \frac{1}{\Delta_y}\delta_x(\Delta_y u_y) - \frac{1}{\Delta_x}\delta_y(\Delta_x u_x) . \tag{12b}$$

The Laplacian operator, which appears in the viscous and diffusive terms (Eqs. 1d, 1e, 5c), is given by

$$\begin{aligned}\nabla^2\psi &= \nabla\cdot\nabla\psi \\ &= \frac{1}{\Delta_y}\delta_x(\Delta_y\delta_x\psi) + \frac{1}{\Delta_x}\delta_y(\Delta_x\delta_y\psi)\ .\end{aligned} \tag{13}$$

The other horizontal finite difference operators appearing in the primitive equations can also be derived in general coordinates. The Coriolis terms are simply given by

$$2\Omega\times\mathbf{u} = -\hat{\mathbf{x}}fu_y + \hat{\mathbf{y}}fu_x\ . \tag{14}$$

The metric momentum advection terms corresponding to the third terms on the left in Eqs. (1a, b) are given by [15]:

$$(uv\tan\phi)/a \rightarrow u_xu_yk_y - u_y^2k_x \tag{15a}$$

$$(u^2\tan\phi)/a \rightarrow u_xu_yk_x - u_x^2k_y \tag{15b}$$

$$k_x \equiv \frac{1}{h_xh_y}\frac{\partial}{\partial q_x}h_y = \frac{1}{\Delta_y}\delta_x\Delta_y \tag{15c}$$

$$k_y \equiv \frac{1}{h_xh_y}\frac{\partial}{\partial q_y}h_x = \frac{1}{\Delta_x}\delta_y\Delta_x \tag{15d}$$

Note that these revert to the standard forms (left of arrows) in spherical polar coordinates, where $h_x = a\cos\phi$ and $h_y = a$. The metric terms in the viscous operators (second and third terms on the right in Eqs. 1d,e) require a more careful treatment. These terms were derived by Williams [12] in spherical coordinates, by applying the thin-shell approximation ($r \rightarrow a$) to the viscous terms expressed in terms of the stress and rate-of-strain tensors. This form was chosen to insure transverse isotropy which implies that for solid rotation the fluid is stress-free. The general coordinate versions of these terms are derived in Appendix A. The results are

$$\begin{aligned}\mathcal{F}_{Hx}(u_x,u_y) = A_M\{&\nabla^2u_x - u_x(\delta_xk_x + \delta_yk_y + 2k_x^2 + 2k_y^2) \\ &+ u_y(\delta_xk_y - \delta_yk_x) + 2k_y(\delta_xu_y) - 2k_x(\delta_yu_y)\}\ .\end{aligned} \tag{16}$$

The formula for $\mathcal{F}_{Hy}(u_y, u_x)$ is the same with x and y interchanged everywhere. It is straightforward to show that these also reduce to the correct form in the spherical polar limit (Eqs. 1d,e).

The exact finite-difference versions of these operators can be easily derived for the various types of staggered horizontal grids A,B,C,D,E [16] given only the forms of the fundamental operators: divergence, gradient, and curl for that type of mesh. Most OGCMs employ either B-type grids (scalars at cell centers, vectors at cell corners) or C-type grids (scalars at cell centers, vector components normal to cell faces). Using standard notation [13] for finite-difference derivatives and averages:

$$\delta_x \psi = \left[\psi\left(x + \Delta_x/2\right) - \psi\left(x - \Delta_x/2\right)\right]/\Delta_x \tag{17a}$$

$$\overline{\psi}^x = \left[\psi\left(x + \Delta_x/2\right) + \psi\left(x + \Delta_x/2\right)\right]/2\,, \tag{17b}$$

the fundamental operators on C-grids have the same form as Eqs. 9, 10, and 12 (there is no transverse averaging of the fundamental derivatives as in the B-grid, but the Coriolis terms (Eq. 14) must be averaged). For the B-type grids, they are given by:

$$\nabla\psi = \hat{\mathbf{x}}\delta_x\overline{\psi}^y + \hat{\mathbf{y}}\delta_y\overline{\psi}^x \tag{18a}$$

$$\nabla\cdot\mathbf{u} = \frac{1}{\Delta_y}\delta_x\overline{\Delta_y u_x}^y + \frac{1}{\Delta_x}\delta_y\overline{\Delta_x u_y}^x \tag{18b}$$

$$\hat{\mathbf{z}}\cdot\nabla\times\mathbf{u} = \frac{1}{\Delta_y}\delta_x\overline{\Delta_y u_y}^y + \frac{1}{\Delta_x}\delta_y\overline{\Delta_x u_x}^x \tag{18c}$$

As discussed in Appendix A, in Bryan-Cox models (which use a B-grid formulation) all viscous and diffusive terms are given in terms of an approximate C-grid discretization in order to ensure they will damp checkerboard oscillations on the scale of the grid spacing.

The implementation of general coordinates in the POP model was relatively simple. POP is a Bryan-Cox type OGCM with an implicit free-surface formulation of the barotropic

mode [17]. It uses a centered-difference spatial differencing scheme that is second-order accurate. The data structure is such that the field arrays are organized as horizontal slabs and are operated on with an outer loop over vertical levels [18]. (This is different than previous versions of the Bryan-Cox model, such as the GFDL MOM model [19], where the data is instead organized as longitude-depth slabs with an outer loop over latitude.) On parallel architectures the horizontal dimensions are spread across processors, while the vertical dimension is held in-processor. For this reason the vertical dimension plays only a minor role in the parallelization, and the subgrid ratio is just that of the horizontal field arrays. POP is designed to be run on a variety of machine architectures, including distributed-memory parallel architectures (both message-passing and data-parallel), as well as serial or vector architectures. General coordinates were easily implemented in the model because of the code structure: for portability all communication is isolated in a small set of stencil and global reduction routines. Most of the stencil coefficients are time-independent and are precomputed and stored. While the stencil coefficients change under our coordinate transformation, the stencil patterns remain the same. Therefore it was only necessary to precompute the new coefficients, leaving the rest of the code unchanged.

3. Analytic Dipole Grids

We now introduce the simplest dipole coordinate system with arbitrarily placed poles that is both analytic and reduces to the standard polar grid as a special case. It is most easily constructed geometrically, as shown in Fig. 1a. Consider an axis (say on the Earth) parallel to the North-South polar axis but displaced by a constant distance, such that it intersects the surface at two points symmetric about the Equator at latitudes $\pm\alpha$. These are the displaced poles, which on the unit sphere are represented by the unit vectors $\hat{\mathbf{r}}_n$ and $\hat{\mathbf{r}}_s$. All coordinate lines in this system are circles determined by the intersection of certain planes with the surface. Associated with each coordinate is a set of planes containing a common axis. The y-coordinate lines are circles determined by the intersection of the

planes containing the displaced polar axis with the surface of the sphere. The x-coordinate lines are circles determined by the set of planes containing another axis, defined as the intersection of the two tangent planes at the displaced-pole points. We will henceforth refer to the x and y coordinate lines as "x-circles" and "y-circles," respectively, and to the corresponding planes as "x-planes" and "y-planes." The system is most naturally described by two angular coordinates χ and τ around these axes. The polar axis will be referred to as the "χ-axis" and the tangent-plane axis as the "τ-axis" (note $0 < \chi < 2\pi$, and $\alpha - \pi/2 < \tau < \pi/2 - \alpha$ with the choice of origin shown in Fig. 1). In the polar limit $\alpha \rightarrow \pi/2$, the χ-axis approaches the true North-South polar axis, the τ-axis moves off to infinity, and the x- and y-circles become lines of constant latitude ϕ and longitude λ, related to χ and τ by: $\chi \rightarrow \lambda$, $\tan\tau \sec\alpha \rightarrow \sin\phi$.

The analytic relations between the new coordinates (χ, τ) and the old are given by the simultaneous solution of the equations for the x- and y-circles passing through an arbitrary point on the surface, represented by the unit vector $\hat{\mathbf{r}} = (\lambda, \phi)$ or (ξ_1, ξ_2, ξ_3) with $\xi_1^2 + \xi_2^2 + \xi_3^2 = 1$ (see Figs. 1b,c):

x-circle:

$$\begin{aligned} &\hat{\mathbf{r}} \cdot \mathbf{b} = b^2 \ , \quad \mathbf{b} = b\hat{\mathbf{n}}_x \\ &b = \sin\tau \sec\alpha \ , \quad \hat{\mathbf{n}}_x = \hat{\boldsymbol{\xi}}_1 \sin\tau + \hat{\boldsymbol{\xi}}_3 \cos\tau \ , \end{aligned} \tag{19a}$$

y-circle:

$$\begin{aligned} &\hat{\mathbf{r}} \cdot \mathbf{c} = c^2 \ , \quad \mathbf{c} = c\hat{\mathbf{n}}_y \\ &c = \sin\chi \cos\alpha \ , \quad \hat{\mathbf{n}}_y = \hat{\boldsymbol{\xi}}_1 \sin\chi - \hat{\boldsymbol{\xi}}_2 \cos\chi \ . \end{aligned} \tag{19b}$$

where b =$|\mathbf{b}|$, c =$|\mathbf{c}|$, and $\mathbf{b}$, $\mathbf{c}$ are the vectors from the center of the sphere to nearest points on the x and y planes, respectively, and $\hat{\mathbf{n}}_x$ and $\hat{\mathbf{n}}_y$ are the corresponding unit vectors in these directions. The orthogonality of the coordinate system is easily demonstrated by

observing that at the surface point $\hat{\mathbf{r}}$, the x and y coordinate circles lie along directions $\hat{\mathbf{x}} \sim (\hat{\mathbf{n}}_x \times \hat{\mathbf{r}})$ and $\hat{\mathbf{y}} \sim (\hat{\mathbf{n}}_y \times \hat{\mathbf{r}})$. The orthogonality immediately follows from

$$\begin{aligned} \hat{\mathbf{x}} \cdot \hat{\mathbf{y}} &\sim (\hat{\mathbf{n}}_x \times \hat{\mathbf{r}}) \cdot (\hat{\mathbf{n}}_y \times \hat{\mathbf{r}}) \\ &= \hat{\mathbf{n}}_x \cdot \hat{\mathbf{n}}_y - (\hat{\mathbf{r}} \cdot \hat{\mathbf{n}}_x)\,(\hat{\mathbf{r}} \cdot \hat{\mathbf{n}}_y) \\ &= \sin\tau \sin\chi - bc = 0\,. \end{aligned} \tag{20}$$

This simple analytic dipole grid can be equivalently constructed using bipolar coordinates on the plane [14] followed by an inverse stereographic map to the sphere (since the stereographic map is conformal, orthogonality is preserved), and it is in fact equivalent to the system obtained from the solution of Poisson's equation on the surface of the sphere with two point charges of opposite sign at the poles.

By simply rotating this coordinate system, dipole grids with arbitrarily located poles can be constructed. We will refer to a coordinate system of this kind as one of the basic Analytic Dipole (AD) grids. Note that a given AD grid is completely specified by the location and orientation of either its polar χ-axis or its tangent-plane τ-axis. An example of such a grid, with the south pole point $\hat{\mathbf{r}}_s$ rotated to the true South Pole, is shown in Fig. 2. This grid fulfills most of the desirable features discussed in the last section, with one exception: it does not have purely zonal coordinates in the Equatorial region, which is desirable for accurate finite-difference dispersion relations of the linear waves. In Section 5 we will discuss how to get around this problem. But first we consider composite generalizations of this basic dipole grid.

4. Composite Dipole Grids

The properties of the basic AD grid make it possible to easily construct global composite grids made up of sections of two or more of them. To show this, we make the following observation:

Theorem: For each pair of circles on the sphere cut by arbitrary planes passing through its surface, there is a unique AD grid with these as coordinate circles.

The proof is by construction. If the circles cross each other, they are both y-circles and intersect at the pole points, which defines the χ-axis. If they do not meet they are x-circles, and the τ-axis is the intersection of the two planes containing them. Either case uniquely defines an AD grid. A pole point is just the limiting case of an x-circle approaching one of the tangent planes, so it also follows that:

Corollary: Given any circle on the sphere and any surface point not lying on it, there exists a unique AD grid with these as one of its x-circles and one of its poles.

This corollary can be used to construct a simple two-patch global composite mesh from two different AD grids which share a common x-circle, one covering the area "inside" and the other the area "outside" this matching circle. Each patch contains one arbitrarily-located pole, which together with the matching x-circle defines the AD grid for that patch. An example of such a grid shown in Fig. 3. In this case the Equator is the matching x-circle, and different AD grids are used in the northern and southern hemispheres, with poles at (95W,50N) and 90S, respectively (so it is just a standard latitude-longitude grid in the south). We note that this type of composite grid is orthogonal everywhere, even on the matching circle. However, as will be discussed below, the finite difference scheme suffers a loss of second-order accuracy in the vicinity of the matching circle.

It is also possible to construct another type of two-patch composite mesh by arranging the AD grids so that the matching circle is an x-circle of one of them and a y-circle of the other. In this case the global grid will have three poles: two lying on the matching circle and one inside one of the patches. An interesting example of such a grid, recently developed independently by R. Bleck, is shown in Figure 4. In this global grid, a standard polar grid is used everywhere south of the matching circle at 65N. The region above 65N is covered with another grid, derived using bi-polar coordinates. As mentioned above, this is equivalent to an AD grid with the two poles located on the matching circle. In this case all three pole points in the global grid can be hidden within land masses. This grid has the advantage

that it is equivalent to a standard polar grid over most of the globe, while retaining the desirable feature that the resolution decreases at high latitudes. One disadvantage of this type of "cross-matched" grid is that it cannot be mapped onto a cyclic 2-D array without folding or cutting, which complicates the data structure as discussed above. The rotated global grid used by Eby and Holloway [1] is another example of a cross-matched composite grid, where the matching circle is at the Equator and the northern rotated grid is used only in the North Atlantic and Arctic oceans. The two patches only meet at the Equator in the Atlantic and hence the Bering Strait is not connected, but (because the global connectivity has been given up) it is possible to lay-out the grid as two patches on a single cyclic 2-D array. For eddy-resolving models, this rotated grid has the disadvantage that it is not possible to focus resolution at high northern latitudes since there are no poles north of the Equator.

Composite grids with three or more AD sections can also be constructed using the above theorem. Imagine several planes passing through the sphere but not intersecting within it. The region of the surface between neighboring circles cut by these planes can be covered with a unique AD grid which contains them as x-circles. If there are $n-1$ planes, then there will be n regions covered by different grids: $n-2$ of them are bounded by two neighboring matching circles, while the two on the ends are bounded by one matching circle and each contain a pole point. This defines an n-patch global composite grid which, like the two-patch grids described above, is everywhere orthogonal. Note that in these n-patch grids the x-coordinates lines are all circles, as in the basic AD grid, however, the y-coordinate lines are no longer simple circles: they are a line of circular arcs linked end-to-end from one pole to the other and joined with equal slopes.

Due to the orthogonality, the slopes of the y-coordinate lines are continuous across matching circles. However, they do not in general have continuous second derivatives there, which makes it impossible to construct a second-order-accurate finite-different scheme (it is possible to arrange for the discontinuity to vanish locally, but this can only happen near

one or two points along the matching circle). This is because a discontinuous change in the second derivative of a coordinate at a point (with respect to some other locally smooth coordinate like λ, ϕ, or ξ_i) leads to a discretization with a sudden change in grid spacing at that point (as is the case across the Equator in Fig. 3), and the leading-order truncation error of typical second-order finite-difference operators is proportional to this change in grid spacing.

To illustrate how the loss of second-order accuracy comes about, consider a simple one-dimensional transformation from some smooth coordinate ξ to a new coordinate $y = f(\xi)$, where for simplicity both ξ and y are scaled to lie within the interval $0 < \xi, y < 1$, and f is the function defining the coordinate transformation. If the interval is discretized with N uniform cells of width $\Delta\xi = 1/N$, then analyzing the truncation error $\epsilon^{(2)} \sim d^2y/d\xi^2 \sim \Delta_j - \Delta_{j-1}$ (where $\Delta_j = y_{j+1} - y_j$) with a Taylor series expansion of $f(\xi)$ around nearby points:

$$f(\xi_{j\pm1}) = f(\xi_j) \pm \frac{1}{N} f'(\xi_j) + \frac{1}{2N^2} f''(\xi_j) \pm \dots , \tag{21}$$

the error is proportional to

$$\Delta_j - \Delta_{j-1} = f_{j+1} - 2f_j + f_{j-1} = \frac{1}{N^2} f''_j + \mathcal{O}\left(\frac{1}{N^4}\right) , \tag{22}$$

where $f_j = f(\xi_j)$. Therefore if f is a smooth function of ξ, and if the system is discretized uniformly in ξ, then the differencing scheme is second-order accurate in the sense that the leading-order truncation error decreases like $\Delta\xi^2 = 1/N^2$. This argument is clearly invalid, however, at points where f has no second derivative; there the differencing scheme is at best first-order accurate. This is precisely what occurs with the y-coordinate lines crossing the matching circles in the composite grids described above. To get around this problem, we consider in the next section the continuum limit of a composite grid with infinitely many AD sections, so that the error is distributed globally (and infinitesimally) across the grid and hence it vanishes.

5. Continuously-Differentiable Dipole Grids

Taking the limit $n \to \infty$ of a continuum of composite grids whose matching x-circles are displaced only infinitesimally from one another, we obtain a new class of dipole grids. To characterize a grid of this type, consider the curve $\mathcal{C}$ defined as the locus of points at the centers of its x-circles, as illustrated in Fig. 5a. Each x-coordinate circle in the grid is determined by the plane normal to some vector $\mathbf{b}$ from the center of the sphere to a point on this curve. Thus the coordinate system is uniquely defined by the curve, and its end points are the poles. Figure 5b shows this curve for the basic AD grid. In this case it is simply an arc of the circle which passes through the origin and the nearest point on the τ-axis with its center halfway between them. As will be shown below, the y-coordinate lines of a grid will have exactly as many derivatives as its associated curve $\mathcal{C}$. Since the truncation error of an nth-order accurate differencing scheme is $\epsilon^{(n)} \sim d^n y/d\xi^n$, it follows that grids whose associated curves $\mathcal{C}$ possess n derivatives at every point will support nth-order differencing schemes.

In this section we consider the class of grids associated with the set of continuously differentiable curves $\mathcal{C}$ connecting two arbitrarily located poles on the sphere and subject to the constraint that its normal planes $\mathbf{r} \cdot \mathbf{b} = b^2$ not intersect within the sphere. We will refer to these as Continuously-differentiable Dipole (or "CD") grids. Each curve $\mathcal{C}$ associated with a CD grid can be characterized by a single parameter s, the distance along the curve measured from some fixed point on it. The equations for the curve and its unit tangent vector $\hat{\mathbf{s}}$ can be expressed in Cartesian coordinates as

$$\mathbf{b} = \hat{\boldsymbol{\xi}}_1 b_1(s) + \hat{\boldsymbol{\xi}}_2 b_2(s) + \hat{\boldsymbol{\xi}}_3 b_3(s) \tag{23a}$$

$$\hat{\mathbf{s}} = \frac{d\mathbf{b}}{ds} , \tag{23b}$$

where b_1, b_2, and b_3 are all smooth functions of s. Given $\mathbf{b}$ and $\hat{\mathbf{s}}$ (or equivalently b_1, b_2, and b_3), all the properties of the grid can be computed in the neighborhood of the x-circle associated with $\mathbf{b}$. The coordinate directions at a point $\hat{\mathbf{r}}_b$ on the x-circle are given by

$$\hat{\mathbf{x}} = \hat{\mathbf{b}} \times \hat{\mathbf{r}}_b \Big/ \left|\hat{\mathbf{b}} \times \hat{\mathbf{r}}_b\right| \tag{24a}$$

$$\hat{\mathbf{y}} = \hat{\mathbf{r}}_b \times \hat{\mathbf{x}} \,. \tag{24b}$$

Consider the infinitesimal annulus on the surface containing the x-circle associated with $\mathbf{b}$, and bounded by the two planes normal to $\mathbf{b}_1 = \mathbf{b} + d\mathbf{b}/2$ and $\mathbf{b}_2 = \mathbf{b} - d\mathbf{b}/2$ (say with $b_1 > b_2$). The area of the annulus is simply given by $dA = 2\pi(b_1 - b_2) = 2\pi db$, provided the planes do not intersect within the sphere. The y-coordinate changes dy across the annulus can be derived analytically given only $\mathbf{b}$ and $\hat{\mathbf{s}}$, since these determine the associated τ-axis and hence the AD grid within the annulus (note that the associated polar χ-axis does not in general pass through the point $\mathbf{b}$ and is not aligned with $\mathbf{b}$ or $\hat{\mathbf{s}}$). The τ-axis is normal to the plane containing $\mathbf{b}$ and $\hat{\mathbf{s}}$, and crosses it at a point $\boldsymbol{\tau}$, which is determined from the simultaneous solution of the equations for the two planes, $\boldsymbol{\tau} \cdot \mathbf{b}_1 = b_1^2$ and $\boldsymbol{\tau} \cdot \mathbf{b}_2 = b_2^2$. Taking the limit $d\mathbf{b} \to 0$ yields

$$\boldsymbol{\tau} \cdot \mathbf{b} = b^2 \tag{25a}$$

$$\boldsymbol{\tau} \cdot \hat{\mathbf{s}} = 2\hat{\mathbf{b}} \cdot \hat{\mathbf{s}} \,, \tag{25b}$$

which can be solved for the two components of $\boldsymbol{\tau}$. We label a given point on the x-circle with the unit vector $\hat{\mathbf{r}}_b$, which in a cylindrical coordinate system with axis $\mathbf{b}$ is $\hat{\mathbf{r}}_b = (b, \lambda_b)$, where λ_b is the angle about the center of the x-circle (see Fig. 5a). The y-coordinate changes at that point are given by the y-circle arc-lengths dy of its associated AD grid across the annulus, and the coordinate changes can be expressed analytically as

$$dx = \sqrt{1 - b^2}\, d\lambda_b \tag{26a}$$

$$dy = \mathbf{G}\left(\mathbf{b}, \hat{\mathbf{s}}, \lambda_b\right) \cdot d\mathbf{b} \,, \tag{26b}$$

where the metric function **G** is a smooth analytic function of its arguments. The algebraic derivation of **G** is outlined in Appendix B. It follows from Eq. 26b that the y-coordinate lines have as many derivatives as the curve $\mathcal{C}$.

Now consider the implications of the condition that the two planes normal to $\mathbf{b}_1$, $\mathbf{b}_2$ not intersect within the sphere, namely: $|\boldsymbol{\tau}| \leq 1$. This leads to $|\mathbf{b}_1 - \mathbf{b}_2|^2 \leq \sin^2\theta_{12}$, (where θ_{12} is the angle between $\mathbf{b}_1$ and $\mathbf{b}_2$). In the limit $d\mathbf{b} \to 0$, this becomes

$$\left|\hat{\mathbf{b}} \times \hat{\mathbf{s}}\right| \leq b\,. \tag{27}$$

That is, the sine of the angle between $\hat{\mathbf{b}}$ and $\hat{\mathbf{s}}$ must be less than b, so the closer they are to the origin the more aligned they must be with one another. This constraint implies that b cannot have a local minimum at any point along the curve $\mathcal{C}$ except at the origin, for if it did then $\hat{\mathbf{b}}$ and $\hat{\mathbf{s}}$ would be perpendicular at that point, violating Eq. 27 for $b > 0$. Therefore the curve $\mathcal{C}$ must pass though the origin, and b must increase monotonically along it from the origin to each pole. Since it can only pass through the origin once, there is exactly one x-circle in the grid which is a great circle, and it is given by the plane normal to $\hat{\mathbf{b}} = \hat{\mathbf{s}}$ at $b = 0$. We refer to this great circle as the "Equator" of that grid. Any computational mesh we construct will have this great circle aligned with the Earth's Equator for the reasons discussed above. So for convenience we will henceforth think of the CD grid as aligned on the Earth in this way and refer to various points by their true latitude and longitude.

To distinguish the two hemispheres, we now redefine b as: $b = |\mathbf{b}|$ in the northern hemisphere but $b = -|\mathbf{b}|$ in the southern hemisphere. Then b must be a monotonically increasing function along the curve from the southern to the northern pole, and $s = s(b)$ is a unique single-valued function. The surface-area integral can then be expressed as:

$$\oint_{\hat{\mathbf{r}}_s}^{\hat{\mathbf{r}}_n} dA = \int_{-1}^{1} 2\pi db = 4\pi\,, \tag{28}$$

where the integral is along the curve C. Furthermore, the functions b_1, b_2, and b_3 (and hence $\mathbf{b}$, $\hat{\mathbf{s}}$, and $\boldsymbol{\tau}$) can be re-expressed as smooth functions of b only, and we may rewrite Eq. 26b as

$$dy = g(b, \lambda_b) db \,, \tag{29}$$

where g is a smooth analytic function of b and λ_b.

For completeness we now specify the fundamental orthogonal variables q_x, q_y of the coordinate system which satisfy q_x = constant on a given x-coordinate line, and q_y = constant on a given y-coordinate line. Since b = constant uniquely identifies a given x-coordinate circle, it is natural to choose $q_x = b$. For the other variable we may choose $q_y = \lambda_0$, the angle (longitude) at which a given y-coordinate line intersects the Equator. In the limit of a simple AD grid, λ_0 is related to the angle χ by $\tan\chi = \sin\lambda_0/(\cos\alpha - \cos\lambda_0)$ (see Fig. 1c). For a general CD grid there is no simple expression for λ_0, but it can be expressed formally in terms of the solution of an integral equation:

$$\hat{\mathbf{r}}_b - \hat{\mathbf{r}}_0 = \int_{\hat{\mathbf{r}}_0}^{\hat{\mathbf{r}}_b} d\mathbf{y} = \int_{\hat{\mathbf{r}}_0}^{\hat{\mathbf{r}}_b} \hat{\mathbf{y}} g(b', \lambda_{b'}) db' \,. \tag{30}$$

The integral is along the y-coordinate line between $\hat{\mathbf{r}}_0 = (0, \lambda_0)$, and $\hat{\mathbf{r}}_b = (b, \lambda_b)$. This equation must be satisfied by a smooth function $\lambda_b = \lambda_b(b, \lambda_0)$ that gives the location of the point $\hat{\mathbf{r}}_b$ as a function of the fundamental coordinates b and λ_0. The differential length elements can therefore be expressed as:

$$dx = h_x(b, \lambda_0) d\lambda_0 \tag{31a}$$

$$dy = h_y(b, \lambda_0) db \tag{31b}$$

$$h_x = \sqrt{1 - b^2}\, \frac{\partial}{\partial \lambda_0} \lambda_b(b, \lambda_0) \tag{31c}$$

$$h_y = g\left(b, \lambda_b(b, \lambda_0)\right) \,, \tag{31d}$$

where h_x and h_y are the metric coefficients (Eq. 7) of the coordinate transformation. The choice of coordinates b, λ_0 is somewhat arbitrary, but note that the finite-difference

operators (Eqs. 9–16) do not depend on this choice, only on the coordinate lengths across the mesh cells $\Delta_i \sim ds_i = h_i dq_i$, so it is not actually necessary to directly solve an integral equation such as Eq. 30 to construct the mesh.

6. Mesh Construction

In order to construct a computational mesh for OGCMs with realistic bathymetry, we are primarily interested in basing it on a CD grid with the north pole $\hat{\mathbf{r}}_n$ displaced smoothly (rather than suddenly as in the composite grid in Fig. 3) into either Asia or North America. For this purpose it is sufficient to restrict the curve $\mathcal{C}$ to lie entirely within the plane containing the origin and the two poles (henceforth referred to as the "pole plane"). In this case the curve can be represented with only two parametric functions instead of three, as in Eq. 23. Furthermore, rather than trying to specify $\mathcal{C}$ for a given grid, it is more convenient to work with an associated surface curve $\mathcal{S}$: the locus of north pole positions $\hat{\mathbf{r}}_n$ of the AD grids associated with each point on $\mathcal{C}$. This makes it easier to parameterize a smooth displacement of the pole to a specific location. With $\mathcal{C}$ constrained to lie in the pole plane, then in the northern hemisphere $\mathcal{S}$ lies along the circular arc between the true North Pole and the northern pole $\hat{\mathbf{r}}_n$, and a point on it can be represented with a single parameter α, the true latitude of the (local) northern pole point on $\mathcal{S}$.

To construct a computational mesh based on an underlying CD grid, we will use a somewhat different approach than that taken in the last section, one which makes use of the corollary rather than the theorem of Section 4. An n-patch composite grid can either be constructed directly by specifying the sequence of $\mathbf{b}$ vectors, or it can be constructed by specifying only the pole angle α of each AD section. This is accomplished as follows. We identify a given matching x-circle by the latitude ϕ_0 (see Fig. 1b) relative to the Equator at which it intersects the shortest y-coordinate line between the poles (which we take to be the origin of the x-coordinate lines, $x = 0$). We choose the pole position α_j associated with the AD grid in the annulus between matching x-circles j and $j+1$ to be some smooth

function $\alpha_j = \alpha(\phi_j)$ (where $\phi_j = \phi_0$ for the jth x-circle). Then, starting with some specified matching x-circle $\mathbf{b}_j$ (usually the Equator, $\mathbf{b} = 0$), successive matching x-circles $\mathbf{b}_{j+1}$ are constructed as the x-circle of the jth AD grid (defined by α_j and $\mathbf{b}_j$, see the corrolary in Sec. 4) which intersects the $x = 0$ line at angle ϕ_{j+1}. The condition that successive x-circles not intersect within the sphere is replaced by the simple requirement that the jth pole α_j lie within (i.e., on the poleward side of) the jth matching x-circle. In this formulation, the coordinate-changes dy at a point $\hat{\mathbf{r}}_{\phi_0}$ on the x-circle labeled ϕ_0, are again given in terms of an analytic function: $dy = f(\phi_0, \alpha, \hat{\mathbf{r}}_{\phi_0})d\phi_0$. Note that since the truncation error $\epsilon^{(2)} \sim d^2y/d\xi^2$ involves a term $(\partial f/\partial\alpha)/(\partial\alpha/\partial\phi_0)$, second-order accuracy requires that α have a continuous first derivative $\partial\alpha/\partial\phi_0$ everywhere.

The algorithm for analytically constructing a discrete mesh for an n-patch composite grid using this method is given in Appendix C. We employ it with a very large value of n when actually constructing global ocean grids. Since it is an analytic construction, the only nonorthogonality introduced is due to roundoff error. In practice we found that if the mesh is computed with 64-bit floating-point numbers, the calculated mesh will converge to about 8 digits of accuracy, provided n is large enough that $\Delta\phi_0 \sim 0.01°$.

Two examples of meshes constructed using this n-patch algorithm are shown in Fig. 6. In this case, the function $\alpha(\phi_0)$ was chosen to have the form:

$$\frac{\pi}{2} - \alpha(\phi_0) = \begin{cases} \left(\frac{\pi}{2} - \alpha_n\right) \sin\left(\frac{\pi\phi_0}{2\alpha_n}\right) & , \quad \phi_0 > 0 \\ 0 & , \quad \phi_0 < 0 \end{cases} , \tag{32}$$

where α_n is the latitude of the northern pole of the CD grid. Thus when $\phi_0 = 0$ (the Equator), $\alpha = \pi/2$ (the true North Pole), and it approaches the northern grid pole from the north $\alpha \to \alpha_n$ as $\phi_0 \to \alpha_n$ approaches it from the south. In the southern hemisphere $\alpha = \pi/2$ everywhere, so it is just the standard polar grid there. Note that this choice for α has a continuous first derivative $\partial\alpha/\partial\phi_0 = 0$ at the Equator, as required for second-order accuracy. In Figure 6a the northern pole has been placed in Canada at (95W,50N), and in Fig. 6b it has been placed in Asia at (85E,50N).

In the case of the standard polar grid, the y-spacing can be chosen to be exactly equal to the x-spacing everywhere, resulting in the familiar Mercator grid with square cells. In a mesh constructed from a general CD grid, however, it is not possible to make every cell square. The meshes in Fig. 6 are Mercator-like grids, in the sense that the y-spacing decreases towards the poles in order to make the cells as nearly square as possible. The mean aspect ratio can be minimized somewhat by choosing a variable x-spacing at the Equator, and focusing more x-resolution near the $x = 0$ line where the resolution in y is already focused. To accomplish this the x-spacing Δx_0 at a given point $\hat{\mathbf{r}}_0 = (0, \lambda_0)$ on the Equator is chosen to be proportional to the distance between poles along the y-coordinate line through that point:

$$\Delta x_0(\lambda_0) = a_n \int_{\hat{\mathbf{r}}_0(\lambda_0)}^{\hat{\mathbf{r}}_n} d\mathbf{y} + a_s \int_{\hat{\mathbf{r}}_s}^{\hat{\mathbf{r}}_0(\lambda_0)} d\mathbf{y} \, . \tag{33}$$

Here the coefficients a_n and a_s are introduced to give different weights to the contributions from the northern and southern hemispheres and are normalized such that $\Sigma_i \Delta x_0 = 2\pi$. We have chosen the coefficients to have the ratio $a_n/a_s = 3$ in order to give greater weight to the more "distorted" northern hemisphere. The grids shown in Figs. 3, 6, 7, and 8 of this article were drawn using the variable x-spacing given by Eq. 33 with $a_n/a_s = 3$. As discussed in Appendix C, the y-spacing was in all cases chosen to be equal to the x-spacing along the y-coordinate lines at $\lambda_0 = \pm 90°$.

Comparing the mesh in Fig. 6a with the two-patch composite grid of Fig. 3, we see that the discontinuity in y-spacing across the Equator has vanished. This grid therefore has essentially all the features we set out to capture in a simple dipole coordinate system. In particular, it has zonal coordinates at the Equator (unlike the grid in Fig. 2), and it can support second-order accurate spatial differencing schemes (unlike the grids in Figs. 3 and 4).

7. Numerical Simulations at $\langle 2/3^\circ \rangle$ and $\langle 1/3^\circ \rangle$ Resolution

As examples of global simulations using a computational mesh based on a CD grid, we present results from two numerical integrations: one a marginally eddy-resolving $\langle 1/3^\circ \rangle$ grid, the other a non-eddy-resolving $\langle 2/3^\circ \rangle$ grid (brackets denote the average resolution of surface ocean points). The horizontal dimensions are 768×512 with 20 vertical levels for the $\langle 1/3^\circ \rangle$ grid, and 384×256 with 32 vertical levels for the $\langle 2/3^\circ \rangle$ grid. These were constructed in the same way as the grids discussed in the last section, with a Mercator grid in the southern hemisphere and using Eqs. 32 and 33. The northern grid pole is displaced into central Canada at (50N, 95W) in the $\langle 2/3^\circ \rangle$, and (50N, 93W) in the $\langle 1/3^\circ \rangle$ grid. These are again Mercator-like grids in the northern hemisphere with square cells along the two y-coordinate lines that cross the Equator at $\lambda_n \pm 90^\circ$ (where λ_n is the latitude of the northern grid pole). Figure 7 shows two spherical projections of the $\langle 2/3^\circ \rangle$ grid. Note in Fig. 7a that the Hudson Bay is closed off since it is too close to the northern grid pole; however, the straits connecting the Beaufort Sea with Baffin Bay are open. The transport in and out of Hudson Bay is believed to be small, so we elected to eliminate it rather than place the pole in Asia and consequently sacrifice resolution in the North Atlantic. Note in Fig. 7b that the x-coordinate lines in the Equatorial region are essentially zonal, and only gradually begin to deviate from this at mid-latitudes. It is of course possible to focus more latitudinal resolution near the Equator by smoothly decreasing the y-spacing there.

Figure 8 shows the resolution and aspect ratio of the $\langle 1/3^\circ \rangle$ grid, plotted in logical space. The resolution is here defined as the square-root of the cell area in kilometers, and the aspect ratio is the ratio of the longer to shorter sides of the cell (note that the $\langle 2/3^\circ \rangle$ grid has just twice the resolution in km of the $\langle 1/3^\circ \rangle$ grid, and the aspect ratio is the same for both). The resolution ranges from 60–65 km in the equatorial Indian Ocean to 10–15 km at both the northern and southern boundaries of the grid (so neither of these will tend to dominate the CFL limits). Compared to a standard Mercator grid with comparable equatorial resolution, it has much finer resolution along the northern coastlines of North

America due to the placement of the pole. In particular, it has enhanced resolution in the region of the Gulf Stream and the Labrador Sea, which is important for resolving the surface and deep western-boundary currents associated with the North Atlantic component of the THC. Note the resolution is not zonally uniform in the southern hemisphere because of the variable x-spacing (Eq. 33). The aspect ratio (Fig. 8b) is less than 1.2 over most of the ocean and is greater than 2 only in small areas along the North American coastline. This grid also has a reasonably large fraction (67%) of ocean vs. land points.

In Figure 9 we show results from numerical simulations using the POP model at the two resolutions. In the initial state the ocean is at rest with respect to the Earth, and the temperature and salinity fields are initialized to the annual-mean climatological values of Levitus [21]. The models are then forced only at the surface: heat and freshwater fluxes are approximated by restoring to annual-mean surface Levitus values with a one-month relaxation time scale, and the annual-mean climatological values of Hellerman and Rosenstein [22] are used for the wind stress. The $\langle 2/3° \rangle$ run uses Laplacian mixing parameterizations (Eqs. 1d,e and 5c) with $A_H = A_M = 1.0 \times 10^3$ m^2/s. The $\langle 1/3° \rangle$ uses the biharmonic forms (Eq. A3 for the viscosity, and the same expression with $F_x \rightarrow \nabla^2$ for the tracer diffusion) which selectively damp only the highest wave numbers. The biharmonic viscosity coefficients were chosen to vary spatially like the cube of the grid spacing, with a value of $A_H = A_M = -3.0 \times 10^{11}$ m^4/s for a cell with the average equatorial grid spacing. The models were integrated with time steps of approximately 50 and 100 minutes for the $\langle 1/3° \rangle$ and $\langle 2/3° \rangle$, respectively; these are limited by the CFL number associated with the gravity-wave speed of the first internal (baroclinic) mode. The integration lengths were 50 years for the $\langle 2/3° \rangle$ and 23 years for the more expensive $\langle 1/3° \rangle$ simulation. This is long enough for the upper ocean to have reached a quasi-equilibrium state: the geostrophic adjustment of the velocities to the density field is for the most part completed for both the barotropic and first baroclinic modes. The deep ocean circulation involves diffusive processes which require much longer (hundreds of years) to equilibrate;

but it is reasonable to make comparisons of quantities such as surface height which mainly reflect the upper ocean circulation. Figure 9 shows the instantaneous sea-surface height η (relative to the mean geoid) at the end of the $\langle 2/3° \rangle$ and $\langle 1/3° \rangle$ runs. The contour interval is 20 cm, and the zero contour is shown as a dotted line (the sign is such that η is positive in the Equatorial Pacific and negative around Antarctica). Contours of constant η lie approximately along streamlines of the flow due to geostrophic balance, and closely-spaced contour lines indicate faster currents. Comparing the $\langle 1/3° \rangle$ and $\langle 2/3° \rangle$ surface heights, we see that the $\langle 1/3° \rangle$ displays very active eddy fields, but in the $\langle 2/3° \rangle$ they are almost completely absent (tropical instability waves appear in both solutions, but they do not stand-out in the surface height field). This is partly because the $\langle 2/3° \rangle$ grid is not fine enough to begin resolving the Rossby radius of the first baroclinic mode and partly because it uses a Laplacian rather than biharmonic formulation of the mixing terms. If biharmonic mixing is used at $\langle 2/3° \rangle$, however, unphysical jets are produced by the western boundary currents, since the eddies that would normally diffuse them are neither resolved nor parameterized. The most eddy-active regions are in and around the strong currents, such as the Agulhas retroflection region below South Africa, where the counter-flowing Agulhas Current and Antarctic Circumpolar Current (ACC) produce large eddies with diameters of 300 km or more. The region off the east coast of Argentina where the Brazil and Malvinas Currents collide head-on also has a strong eddy field. Note that the Gulf Stream is more eddy-active than the Kuroshio Current in the Pacific; this is because the resolution in the Gulf Stream is roughly double that in the Kuroshio (see Fig. 8a).

The large scale features of the height field are quite similar in many respects (for example note the rough agreement of the zero-contour lines), but the ACC and all the subpolar gyres are stronger in the $\langle 1/3° \rangle$ case. The transport through the Drake Passage is about 112 Sv in the $\langle 2/3° \rangle$ and 145 Sv in the $\langle 1/3° \rangle$ model (1 Sv = 10^6 m^3/s); this is reflected by the drop in surface height across the passage of -160 cm in the $\langle 2/3° \rangle$ and -180 cm in the $\langle 1/3° \rangle$ case. The momentum balance in the ACC is different in eddy- and

non-eddy-resolving models, because resolved eddies tend to accelerate the mean flow and more strongly diffuse momentum vertically downward [23], resulting in a stronger, deeper ACC whose path is much more strongly influenced by the bottom topography, as seen in Fig. 9b.

8. Summary

In this paper we have presented a new class of 2-D spherical dipole coordinate systems which allow the northern grid pole to be smoothly displaced into a land mass (such as North America or Asia). These grids are orthogonal and continuously-differentiable and can therefore support higher-order spatial differencing schemes, including the second-order methods used in most current-generation models. Like the standard polar grid, they can be mapped onto a logically 2-D cyclic array, which simplifies the data structure and the implementation on parallel machines. The parameters of the grids can be adjusted to satisfy a number of desirable properties. Mercator-like meshes can be constructed that focus resolution in both coordinate directions near the poles, as desired for resolving the smaller Rossby radius at high latitudes. The mean aspect ratio of grid cells can be minimized by adjusting the grid spacing, as in Eq. (33), although it cannot be arranged so that all mesh cells are square, as in the pure Mercator grid. Each of these grids has exactly one coordinate line which is a great circle, and this can be aligned with the Earth's Equator to obtain a more accurate numerical representation of the linear waves and zonal current systems there. By placing the pole in North America we obtain higher resolution in the Gulf Stream and subpolar North Atlantic, which is useful for modeling the global thermohaline circulation.

To implement such a grid in an OGCM, we have derived the primitive equations in generalized spherical coordinates and presented the finite difference versions of the fundamental operators on Arakawa B- and C-type grids. A simple algorithm for analytically constructing the grid is given in Appendix C. To demonstrate the use of these new grids we have presented results from two global simulations using the POP model: one

with an eddy-resolving $\langle 1/3° \rangle$ average resolution mesh, the other with a non-eddy-resolving $\langle 2/3° \rangle$ mesh. While this new grid scheme has been implemented here in a z-coordinate model, it is independent of the choice of vertical coordinate, and so can be equally well used in isopycnal and sigma-coordinate models.

Acknowledgements: We would like to thank John Dukowicz, Bob Malone, Matt Maltrud, and Sherrill Lysaght for their contributions to various aspects of this work, and we thank Rainer Bleck for providing Fig. 4. This work was supported by the DOE CHAMMP program. Computing resources were provided by the Advanced Computing Laboratory at Los Alamos National Laboratory.

Appendix A: Viscous Terms in Generalized Spherical Coordinates

The derivation of Eq. (16) follows the procedure of Williams [12]. The viscous terms are written in generalized coordinates and expressed in terms of the stress tensor τ_{ij} (related to the rate-of-strain tensor ϵ_{ij} by $\tau_{ij} = 2A_H\epsilon_{ij}$), then the thin shell limit $r \to a$ is applied. Writing the viscous terms as $\mathcal{F}_{Hx}(u_x, u_y) = A_H F_x$, $\mathcal{F}_{Hy}(u_y, u_x) = A_H F_y$, the curvilinear forms of F_x and F_y are given by (see [12], Eqs. 7 and 8):

$$F_x(u_x, u_y) = \frac{1}{h_x h_y}\left[\frac{\partial}{\partial q_x}(h_y \tau_{xx}) + \frac{\partial}{\partial q_y}(h_x \tau_{xy}) + \frac{\partial h_x}{\partial q_y}\tau_{xy} - \frac{\partial h_y}{\partial q_x}\tau_{yy}\right]$$

$$\tau_{xx} = 2\left(\frac{1}{h_x}\frac{\partial u_x}{\partial q_x} + \frac{u_y}{h_x h_y}\frac{\partial h_x}{\partial q_y}\right) \tag{A1}$$

$$\tau_{yy} = 2\left(\frac{1}{h_y}\frac{\partial u_y}{\partial q_y} + \frac{u_x}{h_x h_y}\frac{\partial h_y}{\partial q_x}\right)$$

$$\tau_{xy} = \frac{h_y}{h_x}\frac{\partial}{\partial q_x}\left(\frac{u_y}{h_y}\right) + \frac{h_x}{h_y}\frac{\partial}{\partial q_y}\left(\frac{u_x}{h_x}\right)$$

(for simplicity the coefficient of viscosity A_H which normally multiplies τ_{ij} has been factored out: $\tau_{ij} = 2\epsilon_{ij}$). The expression for F_y is the same with x and y interchanged everywhere. Other terms appearing in the full expressions that involve the vertical z-coordinate, either vanish identically (because the metric coefficients for the horizontal coordinates are independent of the vertical coordinate, and vice versa), or are dropped because they are proportional to the vertical velocity $w = u_z$ which is small $w \ll (u_x, u_y)$ in the thin-shell, shallow-fluid limit. There is also a term $\partial^2 u_x/\partial z^2$ corresponding to the vertical diffusion of the horizontal velocity, which is treated separately in Eq. (1g). Using Eqs. (8) and (15c,d), Eq. (A1) can be rewritten as

$$
\begin{aligned}
F_x &= \delta_x \tau_{xx} + \delta_y \tau_{xy} + k_x \left(\tau_{xx} - \tau_{yy}\right) + 2k_y \tau_{xy} \\
\tau_{xx} &= 2\left(\delta_x u_x + k_y u_y\right) \\
\tau_{yy} &= 2\left(\delta_y u_y + k_x u_x\right) \\
\tau_{xy} &= \delta_x u_y + \delta_y u_x - k_x u_y - k_y u_x \ .
\end{aligned}
\tag{A2}
$$

Inserting the expressions for τ_{ij} and using $\delta_x u_x + \delta_y u_y = 0$ in the thin-shell limit, we arrive after some algebra at the form for F_x given by the terms in brackets in Eq. (16). In the B-grid discretization, this operator (like the simple horizontal Laplacian) contains a checkerboard null space. This is essentially because the underlying gradient operator (Eq. 18a) annihilates $a+/-$ checkerboard field. In Bryan-Cox models the horizontal viscous and diffusion terms (Eqs. 1d–e and 5c) are usually discretized with an approximate C-grid discretization (a five-point stencil rather than the usual nine-point B-grid stencil), where the velocities on the cell faces are taken to be the average of the velocities at the B-grid cell corners. The resulting approximate five-point operator does not contain the null space and hence is able to damp checkerboard noise on the scale of the grid spacing. In POP, the viscous terms (Eq. 16) are also evaluated with an approximate five-point operator analogous to the C-grid implementation. If a biharmonic (i.e, ∇^4 type) parameterization of the viscosity is used, the horizontal viscous terms are approximated by

$$
\mathcal{F}_{Hx}(u_x, u_y) = F_x\left(A_H F_x(u_x, u_y), A_H F_y(u_y, u_x)\right) \ , \tag{A3}
$$

and again, the expression for $\mathcal{F}_{Hy}(u_y, u_x)$ is the same with $x \leftrightarrow y$ everywhere. Here A_H may be spatially varying, as discussed in Section 7.

Appendix B: Algebraic Derivation of the Metric Function G

The metric function **G** defined by Eq. (26b) can be derived algebraically given the parameterization of the curve C, or equivalently $\mathbf{b}$ and $\hat{\mathbf{s}}$ from Eq. (23). First, $\boldsymbol{\tau}$ is determined from the solution of Eq. (25), and from it the two poles $\hat{\mathbf{r}}_n$ and $\hat{\mathbf{r}}_s$ associated

with the local AD grid in the neighborhood of the x-circle at $\mathbf{b}$ can be found. They lie in the $(\hat{\mathbf{b}}, \hat{\mathbf{s}})$ plane at angles $\pm\alpha$ from the vector $\boldsymbol{\tau}$, where $|\boldsymbol{\tau}| = \sec\alpha$ (see Fig. 1b). The equation for the y-plane passing through a given point $\hat{\mathbf{r}}_b$ on the x-circle is given by $\mathbf{r} \cdot \mathbf{c} = c^2$, and the three components of $\mathbf{c}$ can be determined from the solution of the equations

$$\begin{aligned} \hat{\mathbf{r}}_b \cdot \mathbf{c} &= c^2 \\ \hat{\mathbf{r}}_n \cdot \mathbf{c} &= c^2 \\ \hat{\mathbf{r}}_s \cdot \mathbf{c} &= c^2 \ , \end{aligned} \tag{B1}$$

since the points $\hat{\mathbf{r}}_b$, $\hat{\mathbf{r}}_n$ and $\hat{\mathbf{r}}_s$ all lie in the y-plane. Then the coordinate changes dy in an infinitesimal annulus around the x-circle can be derived as follows. Let $\hat{\mathbf{r}}_1$ and $\hat{\mathbf{r}}_2$ label the points where the two bounding planes normal to $\mathbf{b}_1 = \mathbf{b} + d\mathbf{b}/2$ and $\mathbf{b}_2 = \mathbf{b} - d\mathbf{b}/2$ intersect the y-circle associated with $\mathbf{c}$. The system of equations $\hat{\mathbf{r}}_i \cdot \mathbf{c} = c^2$, $\hat{\mathbf{r}}_i \cdot \mathbf{b}_i = b_i^2 (i = 1, 2)$ leads in the limit $d\mathbf{b} \to 0$ to

$$\begin{aligned} d\hat{\mathbf{r}} \cdot \mathbf{c} &= 0 \\ d\hat{\mathbf{r}} \cdot \mathbf{b} &= 2\mathbf{b} - \hat{\mathbf{r}}_b \\ d\hat{\mathbf{r}} \cdot \hat{\mathbf{s}} &= |d\mathbf{b}| \ , \end{aligned} \tag{B2}$$

where $d\hat{\mathbf{r}} = \hat{\mathbf{r}}_1 - \hat{\mathbf{r}}_2$. These equations can be solved algebraically for the three components of $d\hat{\mathbf{r}}$, and expanding to leading order in $d\mathbf{b}$, the metric function $\mathbf{G}$ can be obtained from $dy = |d\hat{\mathbf{r}}| = \mathbf{G} \cdot d\mathbf{b}$. The actual analytic form of $\mathbf{G}$ can be evaluated by resolving the vector equations B1 and B2 in Cartesian coordinates and solving for $\mathbf{c}$ and $d\hat{\mathbf{r}}$ by direct substitution.

Appendix C: Mesh Construction Algorithm

Here we present the algorithm for computing a mesh based on an n-patch composite grid, as outlined in Section 6. For simplicity the algorithm is described here in vector notation (as in Appendix B). The actual solution of the vector equations is most easily accomplished by resolving all vectors in a Cartesian coordinate system (ξ_1, ξ_2, ξ_3) with ξ_3 in the direction of the true polar axis, and ξ_1 lying along the intersection of the equatorial and pole planes (as in Fig. 1).

Given the sequence of angles ϕ_j at which the x-circles intersect the y-coordinate line at $x = 0$, the associated pole angles $\alpha_j = \alpha(\phi_j)$ can be computed from the functional form chosen for α (e.g., Eq. 32). The algorithm starts from some known x-circle (usually the Equator) with normal vector $\mathbf{b}_j$ and with a specified mesh spacing $(\Delta_x)_{ij}$ around the circle (which also determines the grid points $\hat{\mathbf{r}}_{ij}$ on it). Then the next x-circle at $\mathbf{b}_{j+1}$, the points $\hat{\mathbf{r}}_{i,j+1}$ around it, and the arc-lengths $(\Delta_y)_{ij}$ (between $\hat{\mathbf{r}}_{ij}$ and $\hat{\mathbf{r}}_{i,j+1}$) can all be computed from the geometry of the local AD grid defined by $\mathbf{b}_j$ and α_j. The algorithm is outlined below:

Begin loop over j

1) Solve for the two components of the vector $\boldsymbol{\tau}_j$ associated with the AD grid defined by α_j and $\mathbf{b}_j$ using:

$$\begin{aligned} \boldsymbol{\tau}_j \cdot \mathbf{b}_j &= b_j^2 \\ \boldsymbol{\tau}_j \cdot (\hat{\mathbf{r}}_n)_j &= 1 \,, \end{aligned} \tag{C1}$$

where the local northern pole $(\hat{\mathbf{r}}_n)_j$ of the jth AD grid lies in the pole plane at latitude α_j.

2) Find the local southern pole $(\hat{\mathbf{r}}_s)_j$ using $(\hat{\mathbf{r}}_s)_j \cdot \boldsymbol{\tau}_j = 1$.

3) Solve for the next matching x-circle $\mathbf{b}_{j+1}$:

$$\begin{aligned} \boldsymbol{\tau}_j \cdot \mathbf{b}_{j+1} &= b_{j+1}^2 \\ (\hat{\mathbf{r}}_0)_{j+1} \cdot \mathbf{b}_{j+1} &= b_{j+1}^2 \,, \end{aligned} \tag{C2}$$

where $(\hat{\mathbf{r}}_0)_{j+1}$ is the point at latitude ϕ_{j+1} where the x-circle at $\mathbf{b}_{j+1}$ intersects the $x = 0$ line.

Begin loop over i

4) Solve for the three components of the vector $\mathbf{c}_{ij}$ normal to the y-plane which passes through the three points $\hat{\mathbf{r}}_{ij}$, $(\hat{\mathbf{r}}_n)_j$, and $(\hat{\mathbf{r}}_s)_j$:

$$\begin{aligned} \hat{\mathbf{r}}_{ij} \cdot \mathbf{c}_{ij} &= c_{ij}^2 \\ (\hat{\mathbf{r}}_n)_{ij} \cdot \mathbf{c}_{ij} &= c_{ij}^2 \\ (\hat{\mathbf{r}}_s)_{ij} \cdot \mathbf{c}_{ij} &= c_{ij}^2 \ . \end{aligned} \tag{C3}$$

5) Solve for the two components of $\hat{\mathbf{r}}_{i,j+1}$:

$$\begin{aligned} \hat{\mathbf{r}}_{i,j+1} \cdot \mathbf{c}_{ij} &= c_{ij}^2 \\ \hat{\mathbf{r}}_{i,j+1} \cdot \mathbf{b}_{j+1} &= b_{j+1}^2 \ . \end{aligned} \tag{C4}$$

6) Compute the arc lengths along the local x- and y-circles between grid points:

$$\begin{aligned} \cos(\Delta_y)_{ij} &= (\hat{\mathbf{r}}_{ij} - \mathbf{c}_{ij}) \cdot (\hat{\mathbf{r}}_{i,j+1} - \mathbf{c}_{ij}) \,/\, (1 - c_{ij}^2) \\ \cos(\Delta_x)_{i,j+1} &= (\hat{\mathbf{r}}_{i,j+1} - \mathbf{b}_j) \cdot (\hat{\mathbf{r}}_{i+1,j+1} - \mathbf{b}_j) \,/\, (1 - b_j^2) \ . \end{aligned} \tag{C5}$$

End loops over i and j

(to convert the arc lengths from radians on the unit sphere to kilometers on the surface of the Earth, multiply by its radius a). In practice we use this algorithm with a value of n large enough that $\Delta\phi_0 \sim 0.01°$, as discussed in Section 7. To construct a grid with near-square cells along a given y-coordinate line (say with index i_0), we iterate with this small $\Delta\phi_0$ spacing until the integrated y-spacing between the mesh points (i_0, j) and $(i_0, j+1)$ is just greater than the x-spacing between the mesh points (i_0, j) and $(i_0 - 1, j)$. Then the grid cells along the y-coordinate line at i_0 will have an aspect ratio of unity plus a small correction of order 1% for grids with order $\sim 1°$ spacing.

References

[1] Eby, M., and G. Holloway, *Clim. Dyn.* **10**, 241 (1994).

[2] Byran, K., S. Manabe, and R. C. Pacanowski, *J. Phys. Oceanogr.* **5**, 30 (1975).

[3] Semtner, A., J., *J. Phys. Oceanogr.* **6**, 409 (1976).

[4] Augenbaum, J., M., and C. S. Peskin, *J. Comput. Phys.* **59**, 177 (1985).

[5] Baumgardner, J., and P. Frederickson, *Siam J. Numer. Anal.* **22** 1107 (1985).

[6] Cullen, M., *Quart. J. Royal Meterological Society* **100**, 555 (1974).

[7] Heikes, R. P. and D. A. Randall, *Mon. Weather Rev.*, accepted for publication (1995).

[8] Courtier, P., and J.-F. Geleyn,*Q. J. R. Meteorol. Soc.* **114**, 1321 (1988).

[9] Weaver, A., J. Marotzke, P. F. Cummins, and E. S. Sarachik, *J. Phys. Oceanogr.* **23**, 39 (1993).

[10] Bryan, K., The design of numerical models of the ocean circulation, in *Oceanic Circulation Models: Combining Data and Dynamics*, edited by D. L. T. Anderson and J. Willebrand, Kluwer Academic, Norwell, Massachusetts, 1989, p. 474

[11] Pacanowski, R. C., and S. G. H. Philander, *J. Phys. Oceanogr.* **11**, 1443 (1981).

[12] Williams, G. P., *J. Phys. Oceanogr.* **29**, 870 (1972).

[13] Semtner, Jr, A. J., Finite-difference formulation of a World Ocean model, in *Advanced Physical Oceanographic Numerical Modelling*, J. J. O'Brien, Ed., D. Reidel Publishing Company, Norwell, Mass., 1986, p. 187.

[14] Arfken, G., *Mathematical Methods for Physicists*, Academic, New York, 1970.

[15] Haltiner, G. J., and R. T. Williams, *Numerical Prediction and Dynamic Meteorology*, 2nd Ed., John Wiley & Sons, New York, 1980, p. 442.

[16] Arakawa, A., and V. R. Lamb, Computational design of the basic dynamical processes of the UCLA general circulation model, *Methods of Computational Physics* **17**, Academic, New York, 1977, p. 173.

[17] Dukowicz, J. K., and R. D. Smith, *J. Geophys. Res.* **99**, 7991 (1994).

[18] Smith, R. D., J. K. Dukowicz, and R. C. Malone, *Physica D.* **60**, 38 (1992).

[19] Pacanowski, R., K. Dixon, and A. Rosati, The G.F.D.L. Modular Ocean Model users guide version 1.0, GFDL ocean group tech. rep. no. 2 [Available from Geophysical Fluid Dynamics Laboratory, NOAA, Princeton University, Princeton, NJ 08542], 1991.

[20] Bleck, R., private communication, 1994.

[21] Levitus, S., Climatological atlas of the world oceans, *NOAA Prof. Paper 13*, U.S. Govt. Print. Office, Washington, DC, 1982.

[22] Hellerman, S., and M. Rosenstein, *J. Phys. Oceanogr.* **13** 1093 (1983).

[23] Wolf, T. O., E. Maier-Reimer, and D. J. Olbers, *J. Phys. Oceanogr.*, **21**, 236 (1991).

Figure Captions

Figure 1. Geometry of the basic Analytic Dipole (AD) grid. Coordinate lines are circles formed by planes intersecting the surface of the sphere. The x-coordinate circles are formed by the set of planes containing the displaced polar χ-axis, and the y-coordinate circles are formed by the set of planes containing the tangent-plane τ-axis (see text).

Figure 2. Two views of an AD grid with poles at (95W,50N) and 90S. The grid lines are not drawn beyond a small x-circle near each pole.

Figure 3. A two-patch composite dipole grid. The matching circle is the Equator, and the poles are at (95W,50N) and 90S, so it is a standard Mercator grid in the southern hemisphere. The discontinuity in y-spacing across the Equator leads to a loss of second-order accuracy in the spatial differencing scheme.

Figure 4. An example of a cross-matched two-patch composite grid, recently proposed by R. Bleck [20]. A standard polar grid covers the globe below 65N, and a section of an AD grid with poles on the matching circle is used to cover the polar region.

Figure 5. Geometry of the Continuously-differentiable Dipole (CD) grid. Each x-coordinate circle in the grid has an associated vector $\mathbf{b}$ normal to the plane containing the circle. The curve C is the locus of center points of the x-circles in the CD grid, and its endpoints are the grid poles. For every curve C between two arbitrarily located poles satisfying the constraint Eq. (27), there is a unique CD grid which can be constructed from it. The curve C is shown for a general CD grid in a), and for an AD grid in b).

Figure 6. Two examples of CD grids constructed from the parametric function $\alpha(\phi_0)$ given by Eq. (32). In a) the northern grid pole is in Canada at (95W,50N), and in b) it is in Asia at (85E,50N). Both use a standard Mercator grid in the southern hemisphere, and have variable x-spacing at the Equator, as given by Eq. (33).

Figure 7. Two views of the $\langle 2/3° \rangle$ grid. Note the enhanced resolution in the Gulf Stream and subpolar North Atlantic (a), and the zonal x-coordinate lines in the equatorial region (b), which gradually begin to deviate at midlatitudes.

Figure 8. Resolution and aspect ratio of mesh cells in the $\langle 1/3° \rangle$ grid, plotted in logical space. 67% of the mesh cells are ocean points.

Figure 9. Sea-surface height fields at the ends of the (a) $\langle 2/3° \rangle$, and (b) $\langle 1/3° \rangle$, simulations. The contour interval is 20 cm, and the zero-contours are shown as dashed lines (the sign is such that the height is positive in the equatorial Pacific and negative around Antarctica). Strong eddy fields are present in the $\langle 1/3° \rangle$ but not in the non-eddy-resolving $\langle 2/3° \rangle$ simulation. The large-scale features are similar in the two cases, although all the subpolar gyres and the ACC are stronger in the $\langle 1/3° \rangle$ case (see text).

Figure 1.

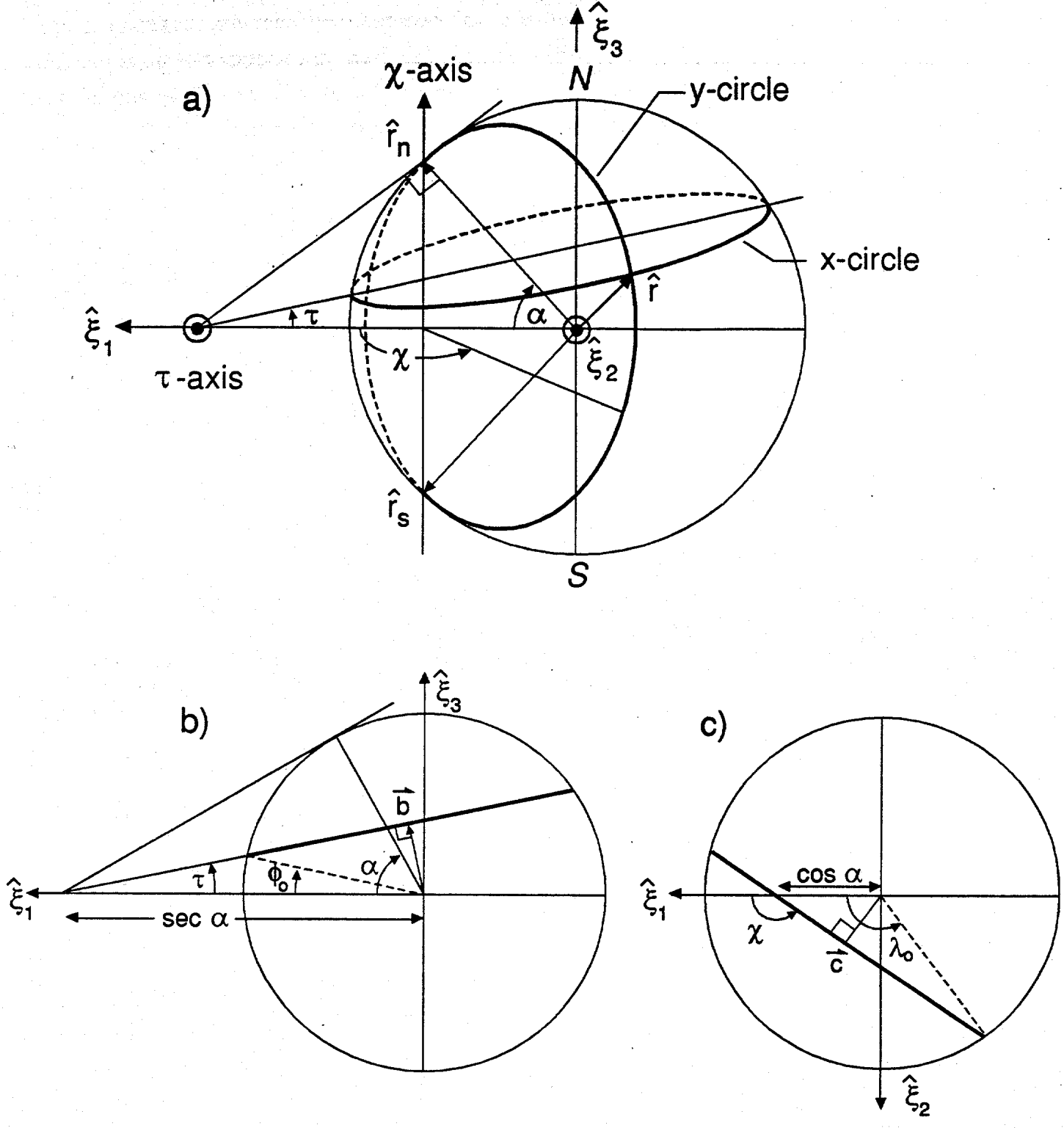
a)
$\hat{\xi}_3$
N
χ-axis
y-circle
$\hat{r}_n$
x-circle
$\hat{r}$
$\hat{\xi}_1$
τ
α
χ
$\hat{\xi}_2$
τ-axis
$\hat{r}_s$
S
b)
$\hat{\xi}_3$
$\vec{b}$
τ
ϕ_o
α
$\hat{\xi}_1$
sec α
c)
cos α
$\hat{\xi}_1$
χ
λ_o
$\vec{c}$
$\hat{\xi}_2$

Figure 2a

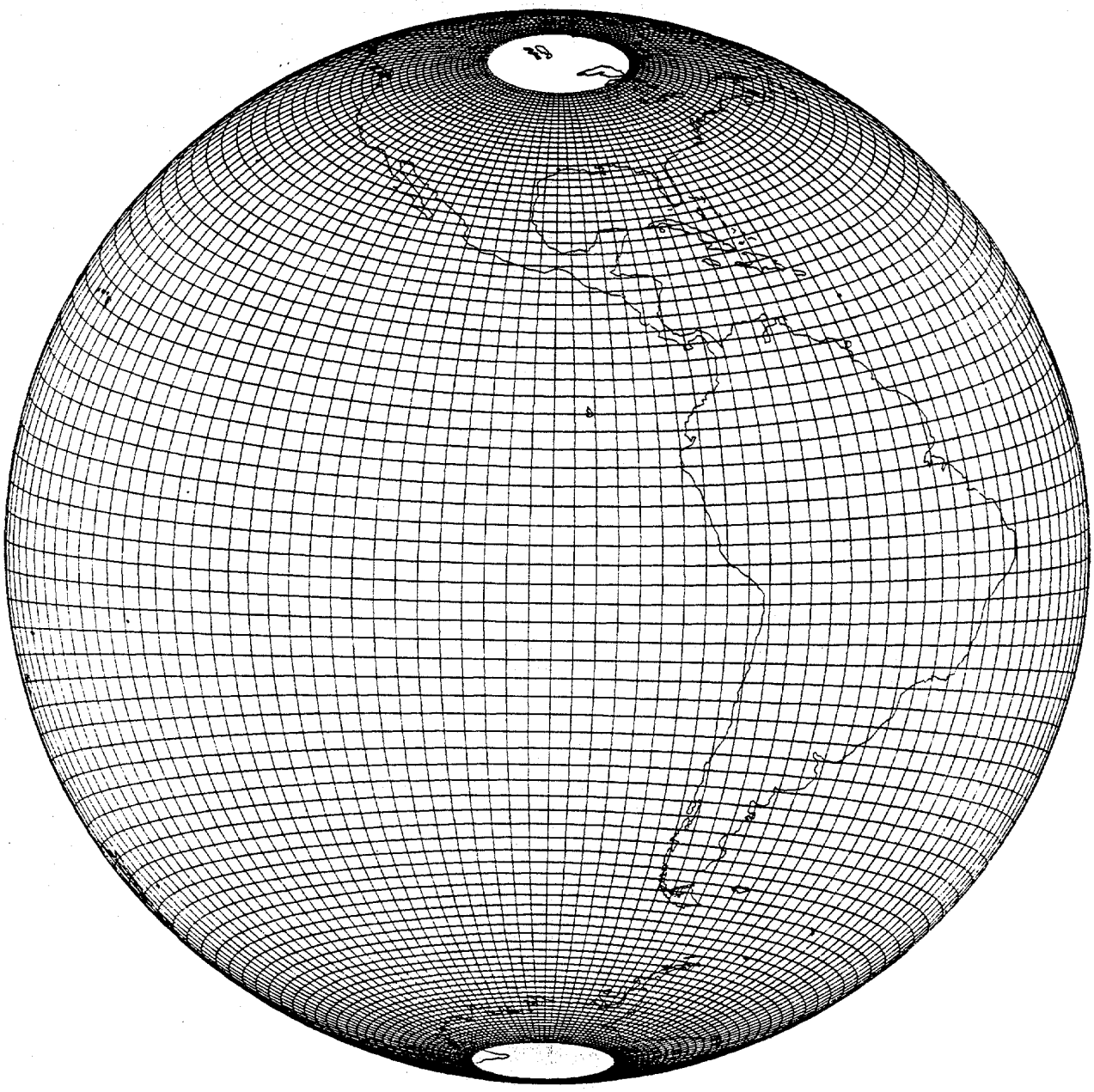

Figure 26

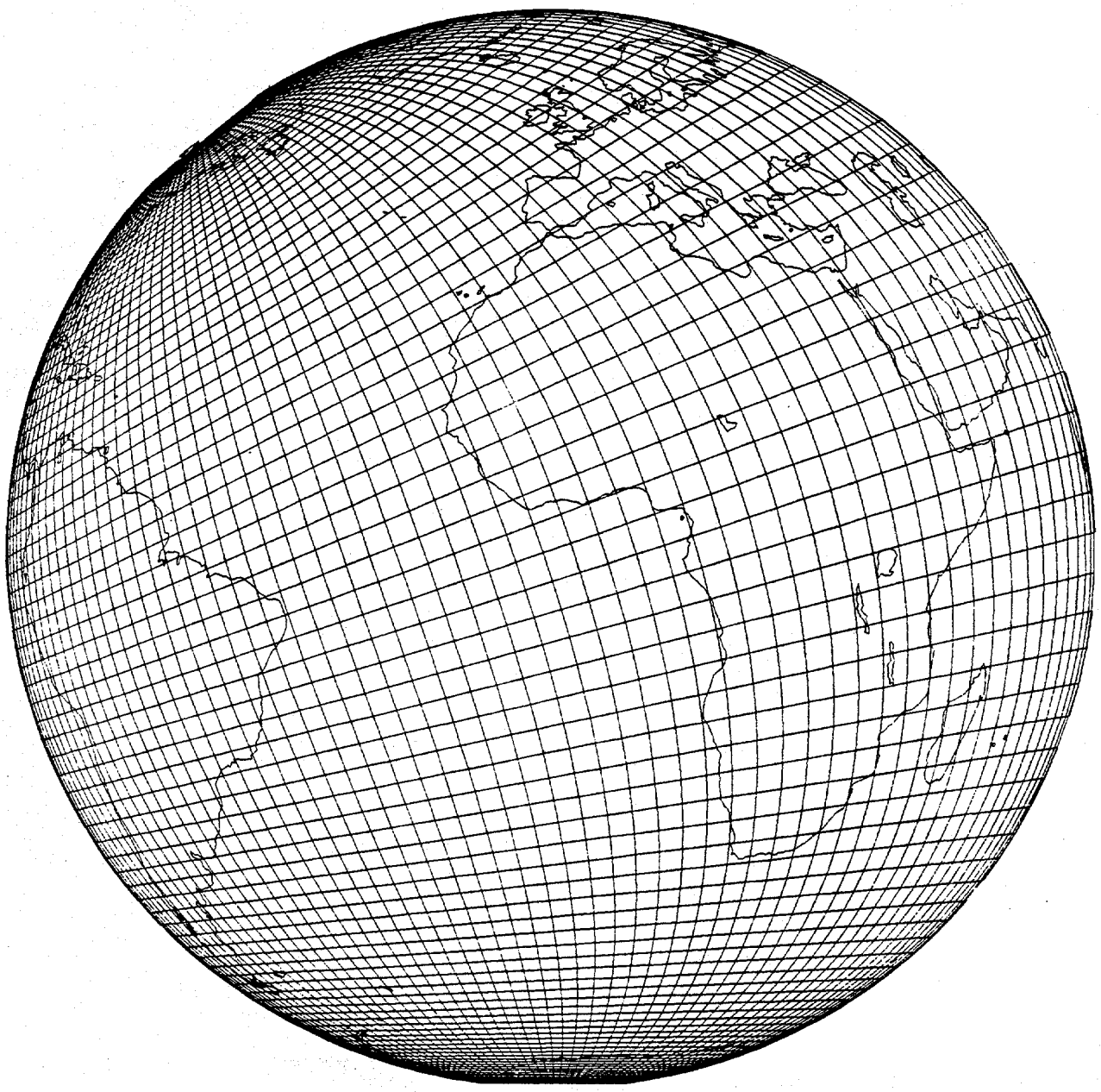

Figure 3

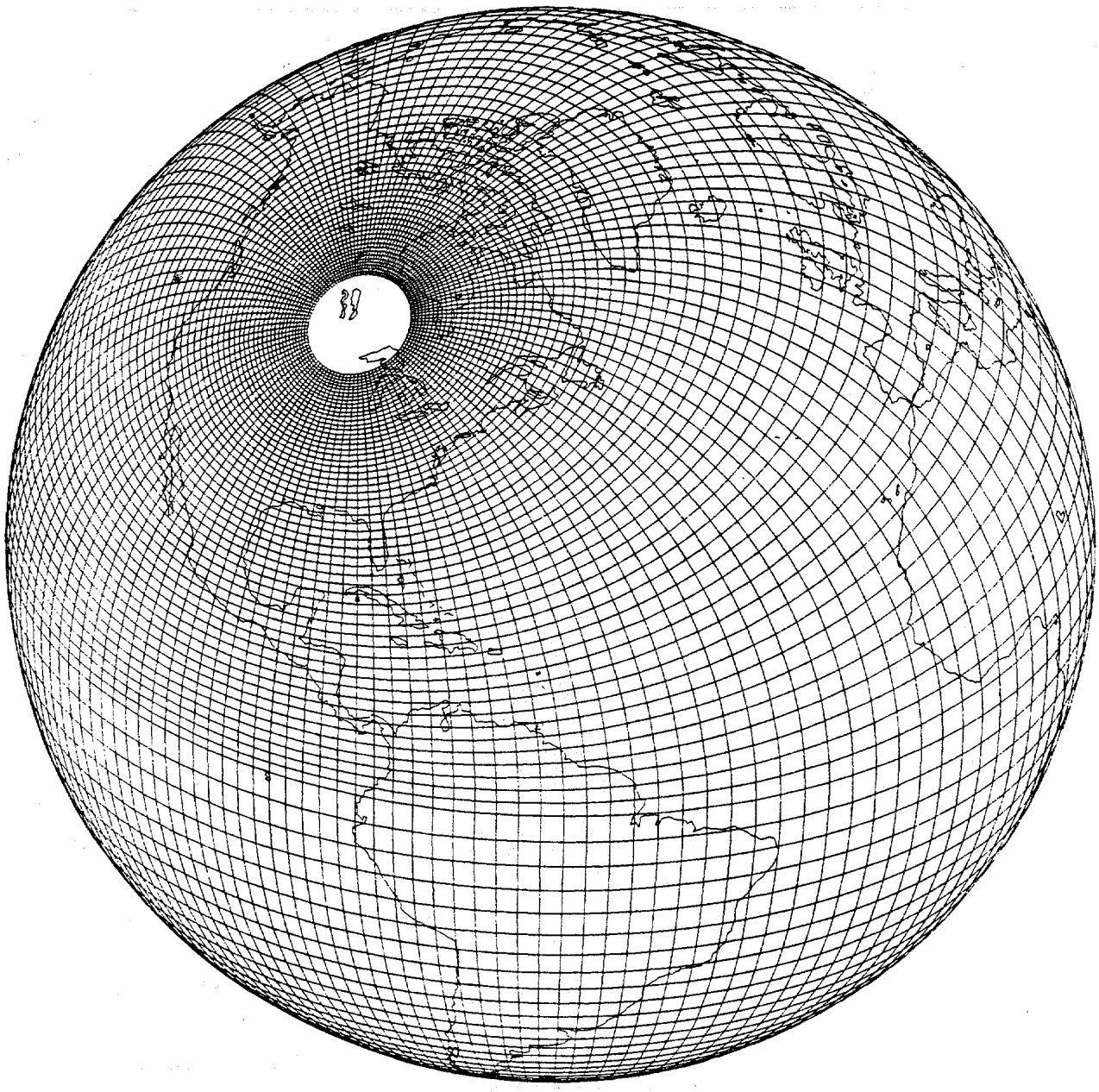

Figure 4

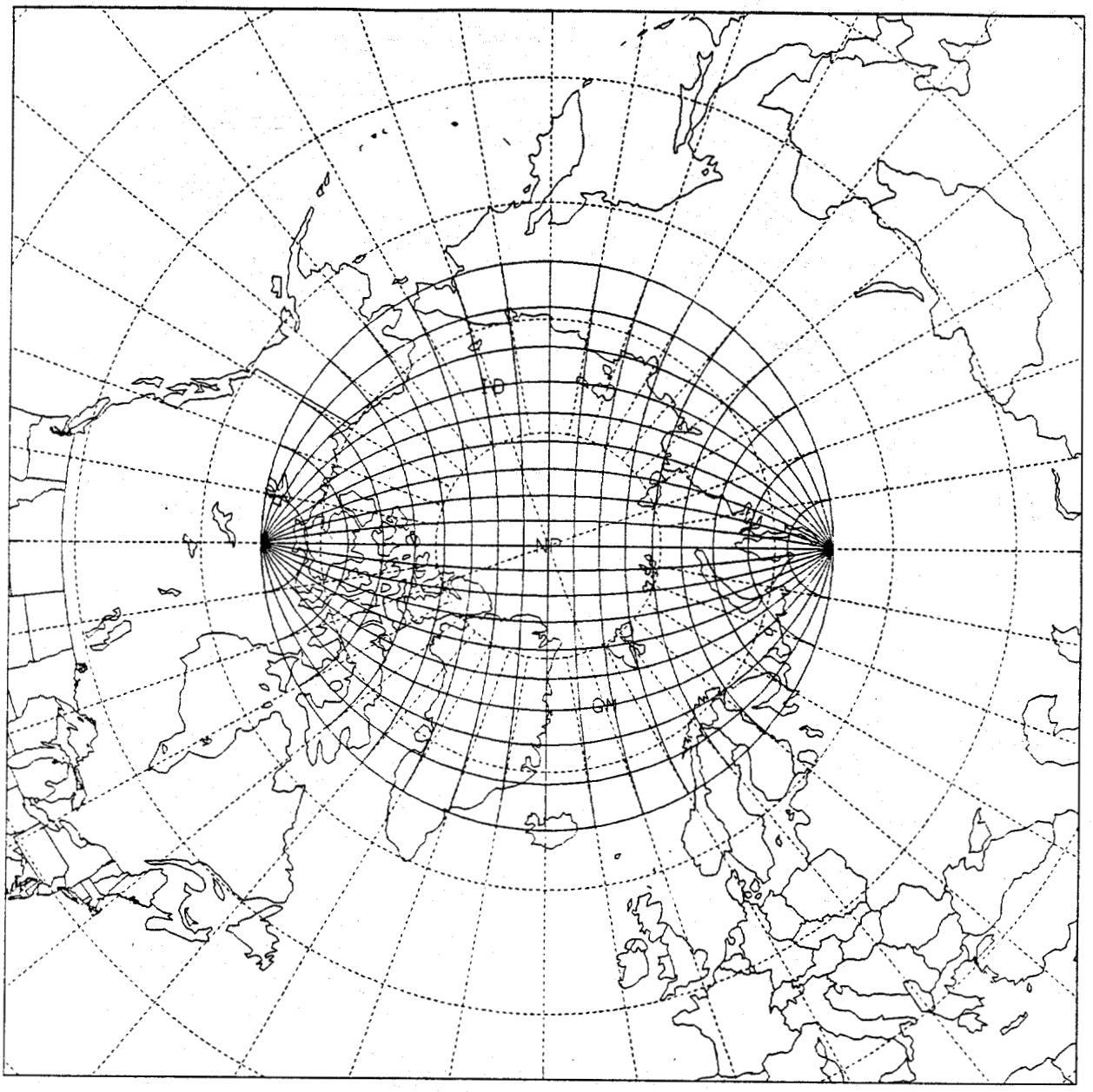

Figure 5

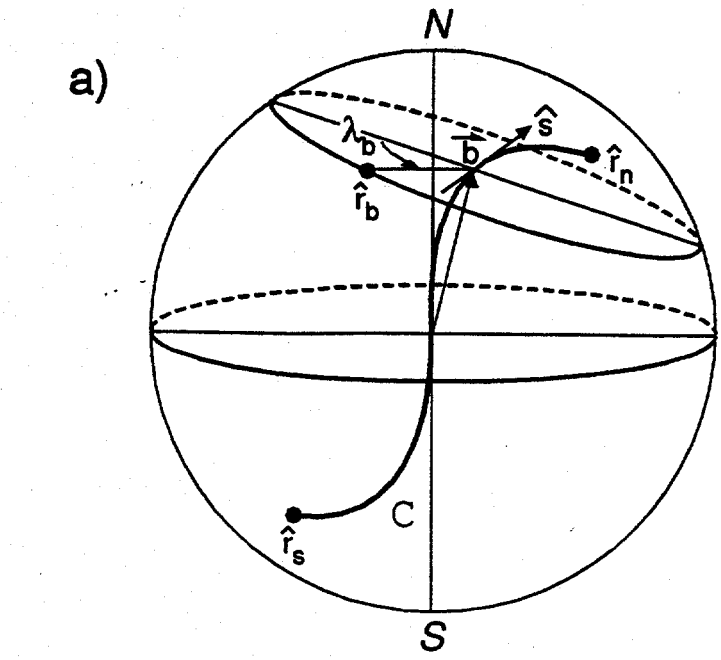
a)
N
S
C
$\hat{r}_n$
$\hat{r}_b$
$\hat{r}_s$
λ_b
$\vec{b}$
$\hat{s}$

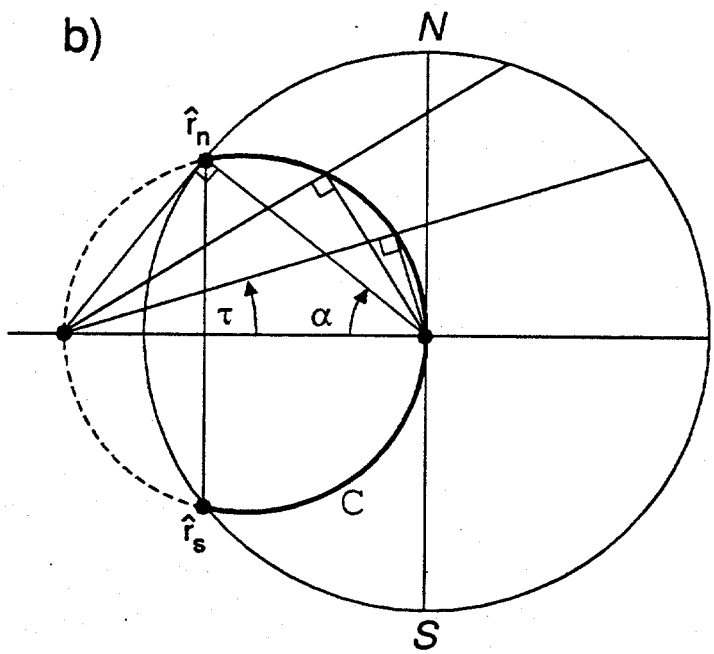
b)
N
S
C
$\hat{r}_n$
$\hat{r}_s$
τ
α

Figure 6a

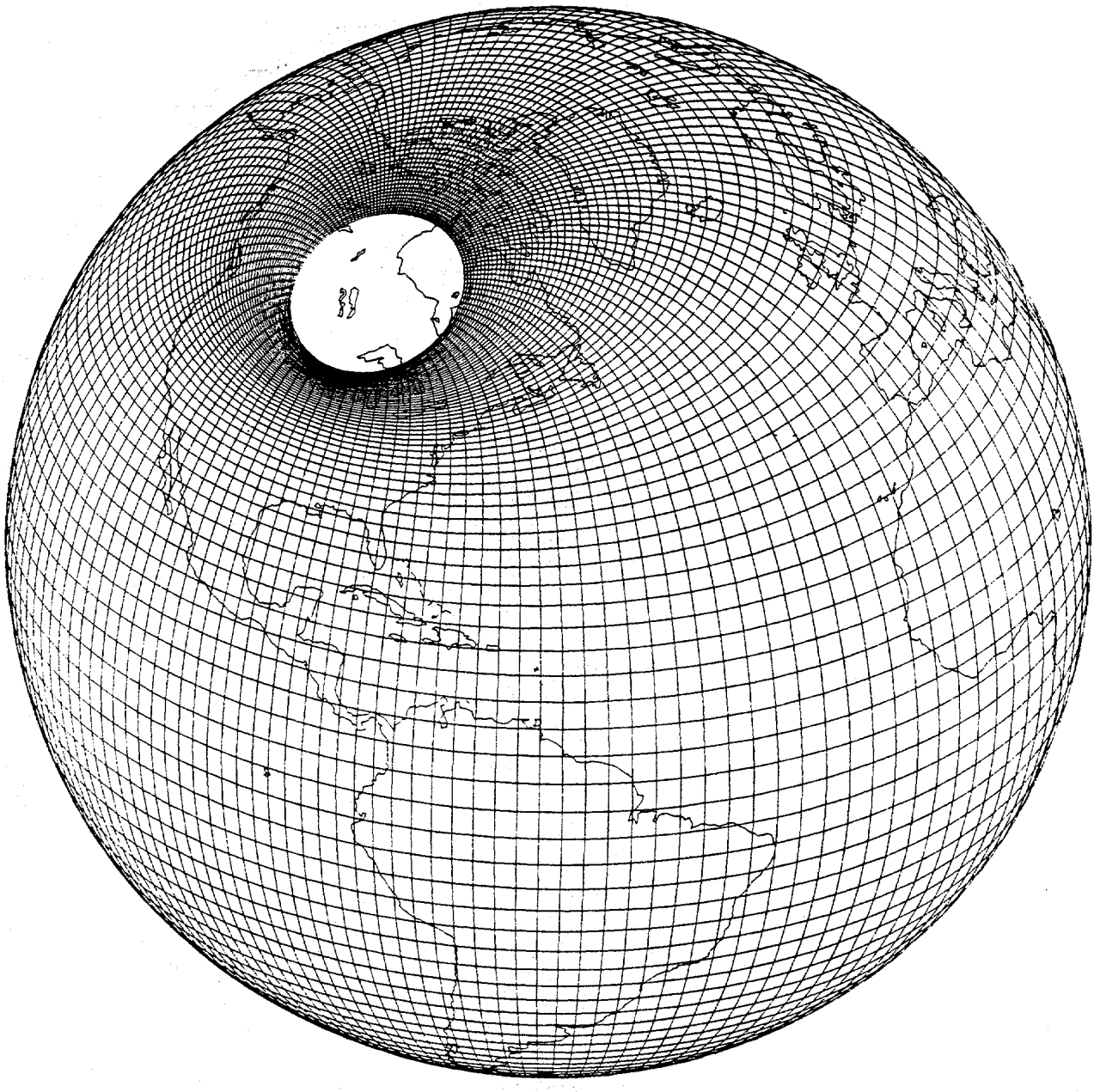

Figure 6

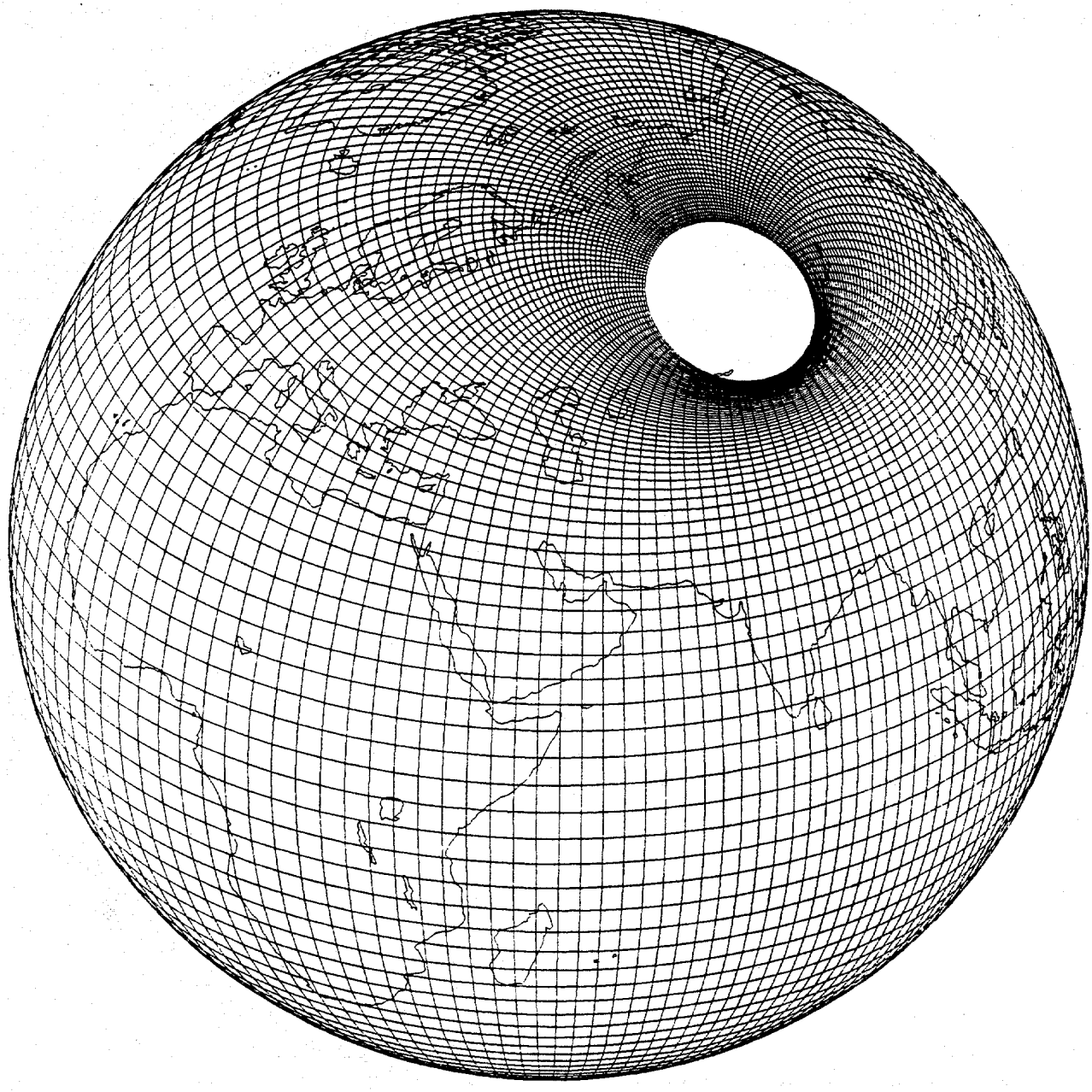

Figure 7a

Figure 7b

Figure 8a

a) Resolution of the <1/3°> Grid

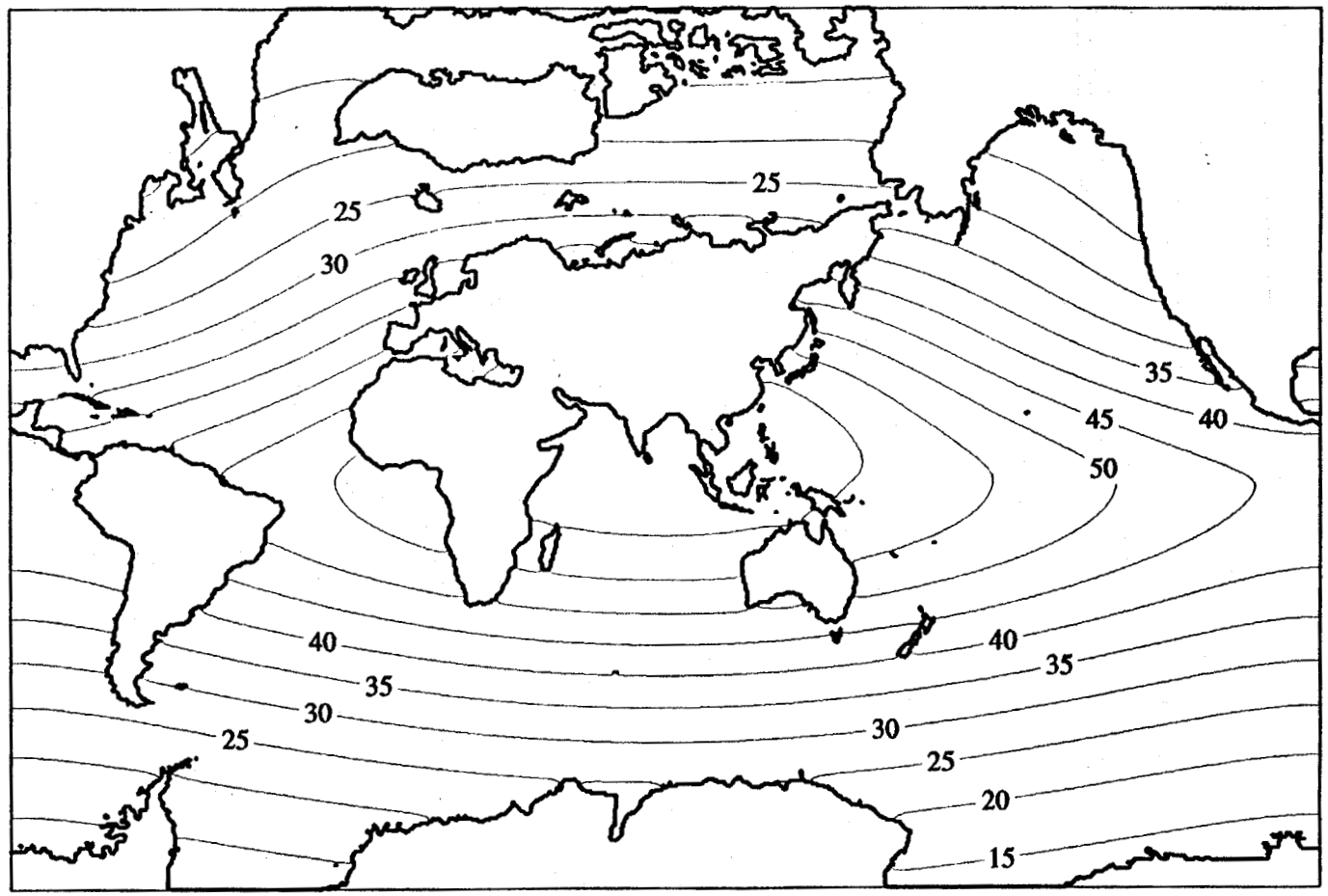

(km)

b) Aspect Ratio of the <1/3°> Grid

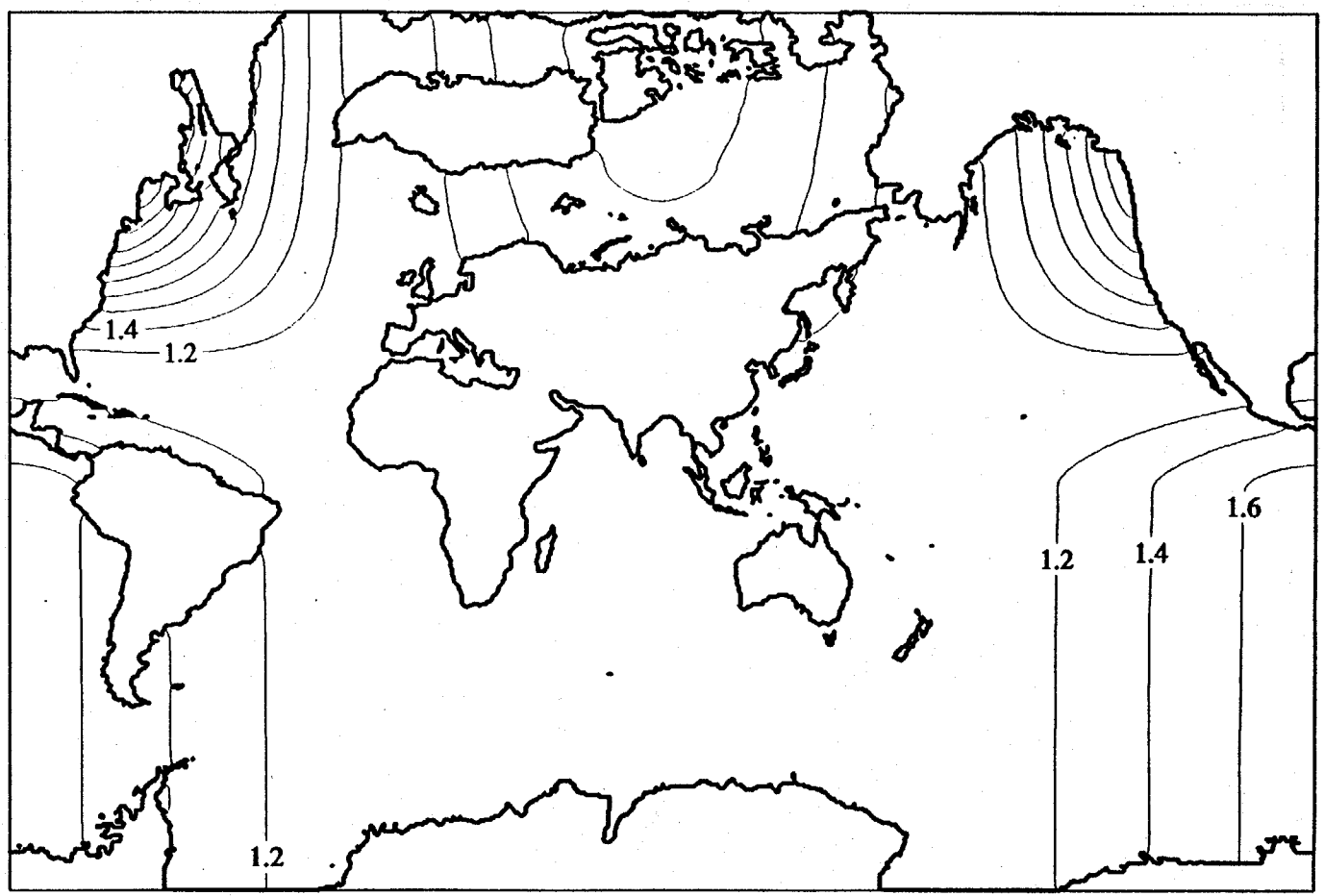

Figure 8b

Figure 9a

Instantaneous Sea-Surface Height (<2/3°> grid, year 50)

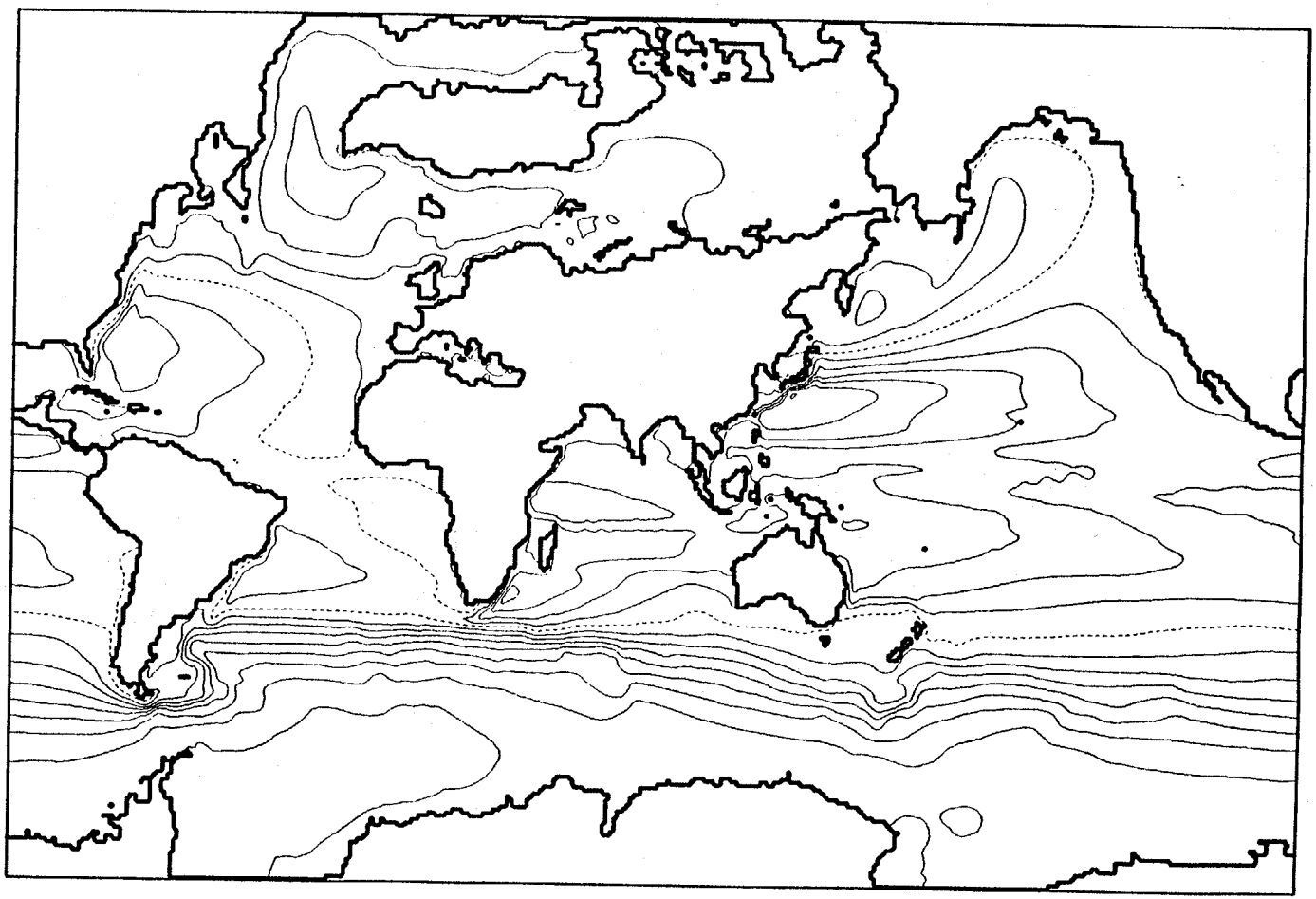

b) Instantaneous Sea-Surface Height (<1/3°> grid, year 23)

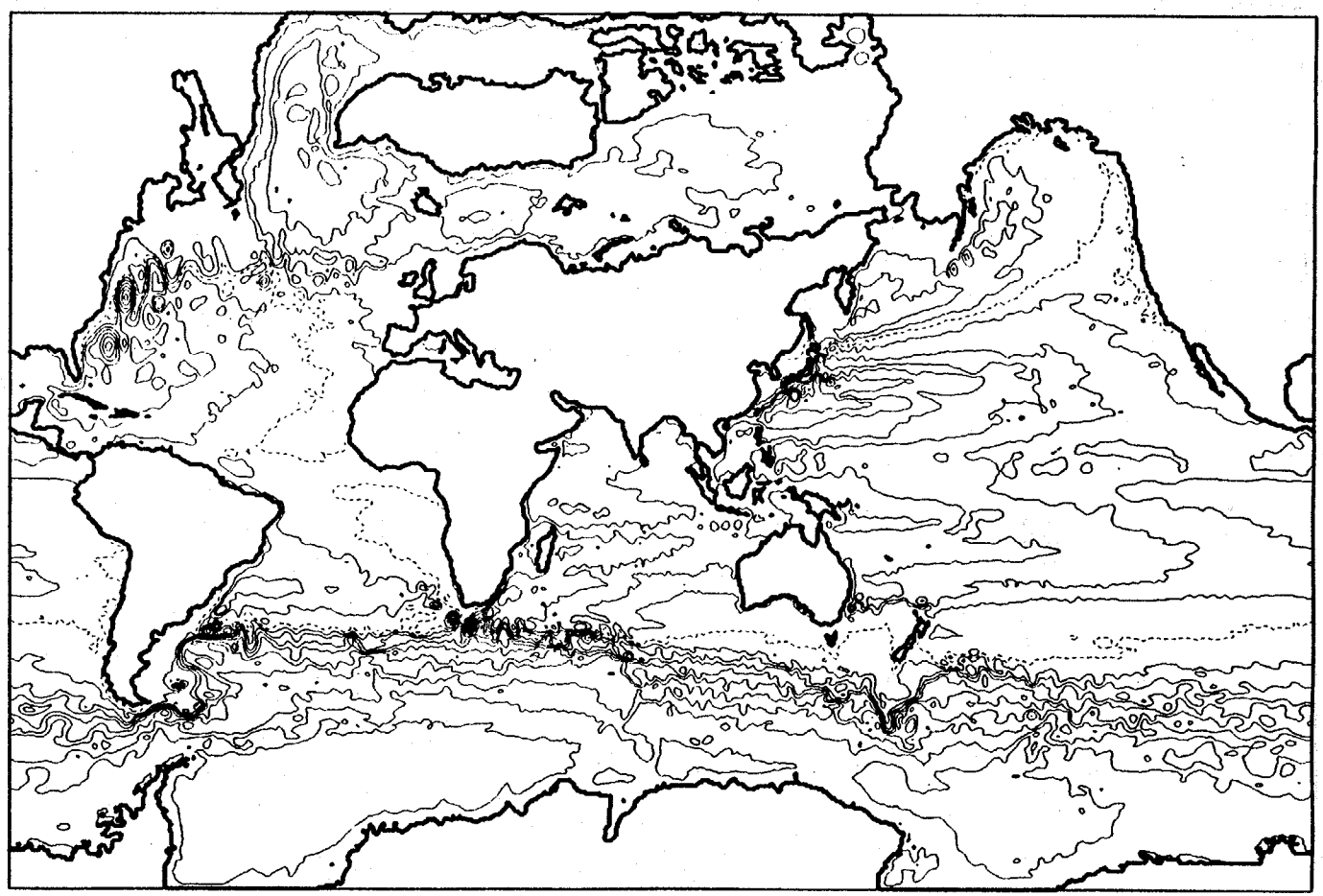

Figure 9b